

Combined topology and build orientation optimization for support structure minimization in additive manufacturing

Luke Crispo, Il Yong Kim*

Department of Mechanical and Materials Engineering, Queen's University, 130 Stuart Street, Kingston, Ontario, K7L 3N6, Canada

* Corresponding author

E-mail address: kimiy@queensu.ca (I. Y. Kim)

Abstract

Additive manufacturing and topology optimization enable the design and fabrication of highly complex components with potential for significant weight savings in the aerospace and automotive industries. Recent research has developed methodologies for combined topology and build orientation optimization to minimize or eliminate overhanging surfaces. However, support structure volume is more representative of additive manufacturing cost, and no methods in literature have derived support structure volume as a smooth and continuous function with respect to element density and build orientation design variables. This paper develops a topology and build orientation optimization approach for additive manufacturing, capable of simultaneously considering support structure volume and overhang area in a multi-objective problem statement to better reflect additive manufacturing cost. To accomplish this, a novel method is proposed for differentiable mapping of element densities from any rotated finite element mesh to a structured mesh aligned with the print direction. Support structure density is calculated layer-by layer based on a supporting region that is applicable for a range of self-supporting threshold angles by varying the aspect ratio of the structured mesh. The proposed method is verified with four numerical problems, including an airplane bearing bracket, demonstrating the approach can be applied to complex, real-world problems. The cost savings obtained through optimization are validated using slicer software, showing that minimizing support structure volume resulted in a 5% to 54% reduction in support material use with a change in print time between +6% to -15% compared to overhang area minimization.

Keywords: design for additive manufacturing, topology optimization, build orientation optimization, support structure volume, overhang angle

1. Introduction

Additive manufacturing (AM) describes a new category of manufacturing methods that fabricate components in a layer-by-layer method, resulting in a significant increase in design freedom compared to traditional subtractive or formative methods. When AM is paired with topology optimization (TO), an approach for computational design generation, it is possible to design and manufacture complex and unconventional structures with improved performance and reduced weight. These technologies ultimately have the potential to improve fuel efficiency in the aerospace and automotive industries (Huang et al. 2016, Verhoef et al. 2018).

The AM process can have difficulty generating material in regions that do not have adequate support from the previously fabricated layers. These regions are typically identified via a self-supporting threshold angle, with surfaces deemed overhanging if they violate the threshold angle for a given AM method (Jiang et al. 2018a). Overhanging surfaces can be generated by printing additional support structures during the AM process and removing these sacrificial supports in a post-processing step (Jiang et al. 2018b). Support structure is a major design criterion for AM because it contributes to cost through three driving factors: material use, build time, and post-processing time (Sabiston and Kim 2019, Olsen and Kim 2020).

Recent research has focused on integrating AM-specific objectives, constraints, and projection schemes into the TO process to produce geometries that are better-suited for AM (Zhu et al. 2021, Ibhadode et al. 2023). Self-supporting approaches use projection schemes (Gaynor and Guest 2016, Langelaar 2017) or strict overhang constraints (Qian 2017, Garaigordobil et al. 2018) to prevent overhanging surfaces from forming, producing designs that can be manufactured without any support structure. However, it is not always possible to produce a fully self-supporting design in problems with complex geometry and loading. Even in cases where support elimination is possible, doing so may result in an undesirable reduction in structural performance or increase in weight. To address this, overhang penalties have been introduced in TO for discouraging unsupported elements from developing without overly constraining design freedom (Ranjan et al. 2017, Thore et al. 2019). While overhangs contribute to an increase in support removal costs and are indirectly related to support structure volume, an ideal approach should directly calculate support structure during optimization. This is because the support structure requirement for each overhanging surface depends on the height from the build plate and the below surfaces that can stop the support column (Mirzendehdel and Suresh 2016). Support structure volume has been incorporated in TO using level set methods (Mirzendehdel and Suresh 2016, Liu et al. 2019) and density-based approaches (Mhapsekar et al. 2018, Ryan and Kim 2019, Xu et al. 2020).

While these support structure TO approaches successfully reduce support volume, they result in larger increases in compliance when compared to self-supporting methods. This is contrary to the expected behaviour as eliminating support is a stricter design requirement compared to reducing support structure. Table 1 summarizes the support volume and compliance changes relative to a baseline design when various methods in literature were applied to a 2D Messerschmitt-Bolkow-Blohm (MBB) beam problem. It is evident that self-supporting and overhang constraint methods eliminate support requirements with a significantly lower increase in compliance relative to support structure methods. It is suspected that this is because support structure formulations overlook some portion of the sensitivity derivation or because the methods are not sufficiently smooth to avoid poor local minimum designs. However, it should be noted the results cannot be directly compared because each approach uses different support or overhang calculations, number of elements, filter radius, and volume fraction limit.

Table 1 Summary of support volume and compliance changes for select methods applied to a 2D MBB beam problem

Reference	Approach	Support Volume (relative to baseline)	Compliance (relative to baseline)
(Gaynor and Guest 2016) (Langelaar 2017)	Projection	-100%*	+19%
	Projection	-100%*	+6%
(Garaigordobil et al. 2018)	Overhang constraint	-100%*	+11%
(Mirzendehdel and Suresh 2016)	Support constraint	-58%	+21%
(Ryan and Kim 2019) (Xu et al. 2020)	Support objective	-36%	+24%
	Support constraint	-34%	+13%

Support structure has also been indirectly minimized through alternative approaches that do not directly calculate overhanging surfaces or support structure during the TO process. These techniques include self-weight manufacturing compliance (Allaire et al. 2017), functionally graded lattice structure design (Panesar et al. 2018), and a virtual skeleton method (Mass and Amir 2017). In addition, support structures themselves have been directly optimized for stiffness and overhang support (Allaire and Bogosel 2018) and optimized simultaneously with structural design (Daynes 2022, Wang and Qian 2022, Wang et al. 2024) for stiffness, heat dissipation, and support removability.

The orientation in which a component is printed, also referred to as the build orientation, can significantly change the number of overhanging surfaces, the support structure volume required for successful manufacturing, and several other factors such as build height, surface roughness, mechanical properties, and residual stresses (Brika et al. 2017, Cheng and To 2019). The selection of an inferior orientation can have a drastic impact on performance metrics, as shown by a compliance gripper example from Langelaar that resulted in 57% difference in deflection between two TO results with opposite build directions (Langelaar 2016b). Despite the importance of the selected print direction, the

previously discussed self-supporting and support volume TO approaches do not consider build orientation during optimization and require the selection of a print orientation in advance, often chosen either arbitrarily or based on intuition. The ideal print orientation may often be unintuitive in complex, 3D problems, and poor selection of build orientation can significantly limit the possible reduction in overhang area or support structure volume. It should also be noted that repeating a fixed-orientation TO for an exhaustive set of orientations is not feasible for practical problems.

Combined topology and build orientation optimization approaches design a structure and print orientation simultaneously to achieve better designs in a streamlined optimization workflow. Self-supporting methods have been integrated into topology and build orientation optimization in various approaches: with additional support volume constraints for interior/exterior edges of the design space (Wang and Qian 2020), through a B-spline parameterized density method (Wang et al. 2022), for the design of self-supported internal voids (Wang 2022), and for the design of assemblies using a neural network-based approach (Chen et al. 2023). Simultaneous topology and build orientation optimization has also been developed for multi-objective optimization of overhang area and build height (Crispo and Kim 2024a).

Combined topology and build orientation optimization for support structure volume is more complex compared to overhang-based approaches because support structure must be calculated as a differentiable function with respect to both build orientation and element density design variables. Fixed-orientation TO methods only require differentiability with respect to element densities and therefore identify support columns by either discretely sorting elements into a set of structured columns at the start of the optimization (Ryan and Kim 2019, Sabiston and Kim 2019) or by requiring the FE mesh to be structured and aligned with the print direction (Mhapsekar et al. 2018, Xu et al. 2020). Topology and build orientation optimization for support structure volume has been implemented in a similar way by discretely sorting elements into columns and relying on finite differencing for sensitivities (Olsen and Kim 2020). However, finite difference sensitivities are highly reliant on selection of perturbation step size, which limits accuracy, reduces stability during optimization, and may require problem specific tuning.

A differentiable support structure volume calculation with respect to build orientation requires discretizing the rotated element density and support structure volume fields into structured vertical columns and horizontal rows (and depth slices for 3D geometries) that are aligned with the build plate. This is essentially equivalent to mapping rotated element densities to a structured mesh and is hereafter referred to density mapping. Support structure minimization has been implemented in a topology and build orientation optimization approach that mapped densities to a structured mesh by smoothly sorting elements into columns and discretely sorting elements by height within each column (Fritz and Kim 2020). This method was limited to 2D quadrilateral meshes and would require significant effort to extend to practical problems with 3D hexahedral and tetrahedral elements. Support structure and part topology have also been designed simultaneously with a pseudo-build orientation optimization approach that used a smooth minimum function to select an orientation from a set of predetermined orientation vectors (Langelaar 2018). This approach mapped densities to a structured mesh using numerical integration, but did not explicitly consider build orientation as a design variable and was only implemented for 2D problems. Therefore, no current methods have the capability to do topology and build orientation optimization using mathematical sensitivity formulation of the important cost metric, support structure volume.

The objective of this paper is to present a new approach for combined topology and build orientation optimization that defines support volume as a smooth and continuation function with respect to build orientation and topology design variables. The methodology matches the performance of self-supporting approaches, while also providing meaningful reductions in support structure volume for complex problems where self-supporting designs are not possible. A multi-objective problem statement simultaneously considers support structure volume and overhanging area to reduce material use and post-processing costs. The remainder of the paper is outlined as follows: Section 2 outlines the topology optimization formulation, density mapping approach, support structure calculation, and sensitivity derivation; Section 3 numerically verifies the approach with four problems; and Section 4 outlines conclusions and future work.

2. Methodology

2.1. Topology and build orientation optimization

Support structure volume Λ and overhang area Ψ are integrated as AM cost metrics into a compliance minimization problem statement in the multi-objective formulation outlined in Eq. (1). Compliance C is calculated by the finite element (FE) solver and scaled by a weighting factor w , which is a user-defined input specifying the importance of structural performance relative to AM cost metrics. Similarly, two cost weighting factors q_Λ and q_Ψ define the relative importance of support structure and overhang area objectives, with $q_\Lambda + q_\Psi = 1$. The ability to alter the weighting of each objective function allows the optimization to generate a unique result that is tailored to the specific cost trade-offs for a given design problem. Each objective is normalized with C_0 , Λ_0 , and Ψ_0 to ensure similar magnitudes.

$$\begin{aligned} \text{minimize : } J(\underline{x}, \theta) &= w \frac{C(\underline{x})}{C_0} + (1-w) \left(q_\Lambda \frac{\Lambda(\underline{x}, \theta)}{\Lambda_0} + q_\Psi \frac{\Psi(\underline{x}, \theta)}{\Psi_0} \right) \\ \text{subject to : } g(\underline{x}) &= \frac{V(\underline{x})}{V_{DS}} \leq \bar{V} \\ \text{where : } K\underline{u} &= \underline{f} \\ x_e &\in [0,1], \quad e = 1, \dots, N_{DS} \\ \theta_1 &\in (-180, 180], \quad \theta_2 \in (-90, 90] \end{aligned} \quad (1)$$

The optimization is constrained to a volume fraction limit \bar{V} , calculated from the volume of the part V and the volume of the design space V_{DS} . A linear static FE analysis is solved each iteration, where K is the global stiffness matrix, \underline{u} is the vector of nodal displacements, and \underline{f} is the vector of applied loads. The topology of the structure is defined through N_{DS} element design variables x_e , while build orientation is determined from two rotation design variables θ_1 and θ_2 (for 3D problems).

This approach uses a density-based TO formulation with a density filter to smooth element design variables \underline{x} and to avoid numerical checkerboarding in the filtered density field $\bar{\underline{x}}$ (Sigmund 2007). Equation (2) outlines the filter calculation, where d_{ei} is a weighting term based on the distance $\|\underline{s}_{ei}\|$ between the e -th element and i -th neighbouring elements within the filter radius R_F . The distance is calculated from the vector $\underline{s}_{ei} = \underline{r}_i - \underline{r}_e$, where \underline{r}_i and \underline{r}_e are element centroid locations extracted from the nodal coordinates of the FE mesh. The filtering equation also scales density based on element volume v_i , which is needed when solving problems with unstructured meshes. While this density filter was effective for all problems tested in this manuscript, a Helmholtz-type partial differential equation filter (Lazarov and Sigmund 2011) could be implemented to efficiently solve large scale TO problems (with more than one million elements).

$$\bar{x}_e(\underline{x}) = \frac{\sum_{i \in N_e} d_{ei} v_i x_i}{\sum_{i \in N_e} d_{ei} v_i} \quad (2)$$

$$d_{ei} = \max(0, R_F - \|\underline{s}_{ei}\|) \quad (3)$$

The domain extension approach is used during filtering to remove undesired boundary effects of the filtering process (Clausen and Andreassen 2017). A layer of void elements is added around the exterior boundaries of the component in the FE model, and solid elements are placed at loads and supports locations (Sabiston and Kim 2019).

Filtered densities are calculated for void elements in addition to the design space elements using Eq. (2), whereas the filtered density is set equal to one for solid elements. This results in a physical density field including all designable, void, and solid elements of length $N_p \geq N_{DS}$. The void boundary elements and fixed load/support elements are included in the N_e neighbouring elements set in the filter calculation in Eq. (2), using a value of $x_i = 0$ for void elements and $x_i = 1$ for solid elements (as these elements do not have design variable values).

Filtered element densities are thresholded in Eq. (4) using a smooth Heaviside function to improve discreteness in the physical density field ρ . The physical densities are used for calculation of all objective and constraint functions (Wang et al. 2011). The smooth Heaviside function is defined in Eq. (5), with the parameter β_\square denoting the slope and η_\square denoting the threshold limit. The smooth Heaviside function is nearly linear for small β_\square values and approaches a discrete step function for large β_\square values. In the physical density calculation, the threshold limit is defined as $\eta_\rho = 0.5$ and the slope parameter is initialized at $\beta_\rho = 1$ and doubled in subsequent optimization phases as described in Section 3. Future references to this S_H^\square function are denoted by a unique \square superscript and use different parameter values as outlined in Table B.1 of Appendix B.

$$\rho_e(\bar{x}) = S_H^\rho(\bar{x}_e) \quad (4)$$

$$S_H^\square(a) = \frac{\tanh(\beta_\square \eta_\square) + \tanh(\beta_\square(a - \eta_\square))}{\tanh(\beta_\square \eta_\square) + \tanh(\beta_\square(1 - \eta_\square))} \approx \begin{cases} 1, & a > \eta_\square \\ 0, & a < \eta_\square \end{cases} \quad (5)$$

The stiffness of each element E_e is updated in Eq. (6) using the Solid Isotropic Material with Penalization (SIMP) method (Bendsoe and Sigmund 1999). Physical densities are penalized with the penalty factor p to discourage intermediate density elements during optimization. The stiffness is interpolated from the material Young's modulus E_0 and a minimum stiffness E_{min} is defined to avoid a singular stiffness matrix.

$$E_e(\bar{x}) = E_{min} + \rho_e^p(E_0 - E_{min}) \quad (6)$$

The build direction vector is determined from a reference vector \tilde{b} , pointing in the $+y$ direction, rotated by θ_1 about the z axis and by θ_2 about the x axis, as shown in Figure 1. This rotation is calculated in Eq. (7), where $[\tilde{b}] = [0, 1, 0]^T$ and the rotation matrix R is defined in Eq. (8). Any build direction can be reached through these two rotations within the rotational design variable limits specified in Eq. (1).

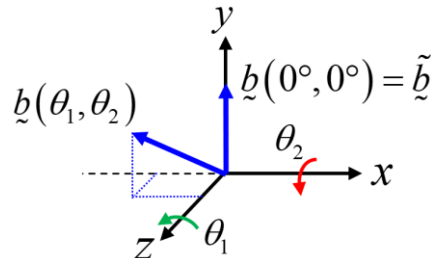


Figure 1 Definition of build direction vector from two rotational design variables

$$\tilde{b}(\theta) = R\tilde{b} \quad (7)$$

$$[R(\theta)] = \begin{bmatrix} \cos \theta_1 & -\sin \theta_1 & 0 \\ \cos \theta_2 \sin \theta_1 & \cos \theta_2 \cos \theta_1 & -\sin \theta_2 \\ \sin \theta_2 \sin \theta_1 & \sin \theta_2 \cos \theta_1 & \cos \theta_2 \end{bmatrix} \quad (8)$$

Overhang area and support structure volume metrics are calculated within the topology and build orientation optimization framework in terms of the build orientation vector $\underline{b}(\theta)$, and the centroid position \underline{r}_e and physical density $\rho_e(x)$ of each element.

2.2. Overhang area calculation

A detailed derivation of the overhang area objective in topology and build orientation optimization is presented by Crispo and Kim (Crispo and Kim 2024a), but is summarized here for completeness. First, the spatial gradient vector of element density and its magnitude are calculated in Eqs. (9) and (10), where $\varepsilon_\psi = 0.01$ is a small non-zero parameter to smooth the magnitude calculation. This calculation approximates the spatial gradient using a weighted average of element density and the distances from the e -th element to the i -th neighbouring elements within the interface radius R_I as depicted in Figure 2.

$$\nabla \rho_e(x) = \frac{\sum_{i \in N_e} v_i \rho_i S_{ei}}{\sum_{i \in N_e} \|S_{ei}\| v_i} \quad (9)$$

$$\|\nabla \rho_e(x)\| = \sqrt{\sum_{j=1}^3 (\nabla \rho_e)_j^2 + \varepsilon_\psi^2} - \varepsilon_\psi \quad (10)$$

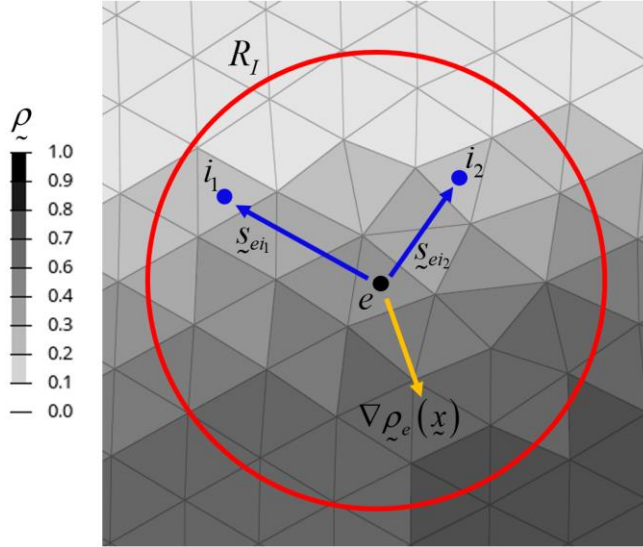


Figure 2 Calculation of element density spatial gradient using neighbouring element densities

The spatial gradient magnitude is used to calculate the elemental contribution to surface area in Eq. (11), where $a_\phi = 2$ is a scaling factor for the Heaviside output.

$$\phi_e(x) = \frac{v_e^{2/3}}{a_\phi} S_H^\phi (\|\nabla \rho_e\|) \quad (11)$$

The cosine of the angle between the surface and the build direction vector is calculated from the spatial gradient vector in Eq. (12). The elemental contribution to overhang area when printing on a raft (which considers the build plate as overhanging) is calculated in Eq. (13) by comparing the surface angle to the self-supporting threshold angle $\bar{\alpha}$ by

setting the Heaviside threshold parameter to $\eta_\psi = \cos \bar{\alpha}$. The result is multiplied by surface area to only consider overhanging elements that lie on the surfaces of the part.

$$\cos \alpha_e(x, \theta) = \frac{\nabla \rho_e}{\|\nabla \rho_e\| + \varepsilon_\psi} \cdot b \quad (12)$$

$$\psi_e^{\text{raft}}(x, \theta) = \phi_e S_H^\psi(\cos \alpha_e) \quad (13)$$

The overhanging indicator ψ_e^{raft} includes all overhanging elements, even if they lie on the build plate. However, some AM methods, such as fused filament fabrication (FFF) (also known as fused deposition modelling), print components directly on the build plate. In this case, the bottom surfaces do not require support material or post processing and should therefore be excluded from the overhang area calculation. A new build plate indicator is defined to identify elements that lie on or below the build plate. First the height of each element in the print direction is calculated in Eq. (14) and the centroid of the part in the build direction is identified with Eq. (15). The distance of each element from the centroid (in the print direction) is calculated in Eq. (16) and weighted by thresholded physical density, resulting in a field that is zero for void elements and zero for elements in line with the centroid. This term is negative for elements below the centroid, decreases towards the bottom of the part, is positive for elements above the centroid, and increases towards the top of the part.

$$h_e(\theta) = r_e \cdot b \quad (14)$$

$$\bar{h}(x, \theta) = \frac{\sum_{e \in N_p} h_e \rho_e}{\sum_{e \in N_p} \rho_e} \quad (15)$$

$$\hat{h}_e^\psi(x, \theta) = (h_e - \bar{h}) S_H^h(\rho_e) \quad (16)$$

The distance from the centroid to the bottom of the part B^ψ (in the print direction) is calculated in Eq. (17), using a smooth minimum of the density-weighted distance field \hat{h}^ψ . A generic smooth maximum and minimum function is defined in Eq. (18) for a generic input vector c . The α_\square parameter controls the function smoothness, with positive values corresponding to a maximum function and negative to a minimum function.

$$B^\psi(x, \theta) = S_{\text{MIN}}^\psi(\hat{h}^\psi) \quad (17)$$

$$S_{\text{MAX/MIN}}^\square(c) = \frac{\sum_{i \in N} c_i \exp(\alpha_\square c_i)}{\sum_{i \in N} \exp(\alpha_\square c_i)} \approx \begin{cases} \max(c), & \alpha_\square > 0 \\ \min(c), & \alpha_\square < 0 \end{cases} \quad (18)$$

A build plate indicator field μ is calculated in Eq. (19) by comparing the distance of each element from the element centroid ($h_e - \bar{h}$) to the distance to the bottom of the part from the centroid B^ψ . A smooth Heaviside function results in an indicator value of 0 for elements below the build plate and a value of 1 for elements above the build plate. This term can therefore be multiplied by the raft overhanging area to eliminate overhanging elements below the build plate in Eq. (20), yielding the overhanging area when printing on the build plate. The distance terms used to calculate the build plate indicator are shown in Figure 3, with the dotted blue line showing the build plate location.

$$\mu_e(x, \theta) = S_H^\mu(h_e - \bar{h} - B^\psi) \quad (19)$$

$$\psi_e^{\text{plate}}(x, \theta) = \psi_e^{\text{raft}} \mu_e \quad (20)$$

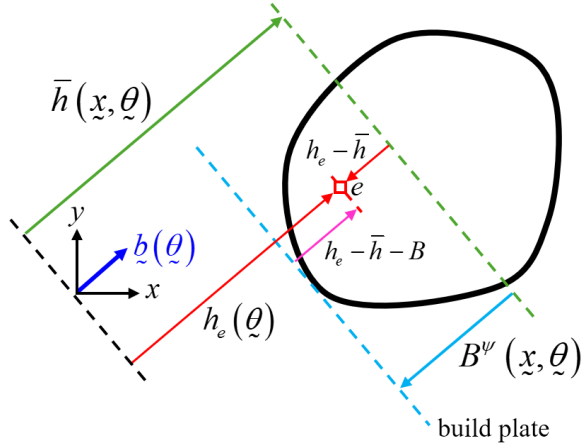


Figure 3 Depiction of distance terms used to calculate the build plate indicator

Finally, the total overhanging area of the part is calculated by summing the element-level overhanging field in Eqs. (21) and (22) for printing on a raft and build plate, respectively. Readers are referred to (Crispo and Kim 2024a) for the sensitivity expressions and finite difference verification of the overhanging area calculation. An in-depth investigation into the differences between optimizing for printing on a raft compared to printing on the build plate is available in (Crispo and Kim 2024b).

$$\Psi^{\text{raft}}(\tilde{x}, \tilde{z}) = \sum_{e \in N_p} \psi_e^{\text{raft}} \quad (21)$$

$$\Psi^{\text{plate}}(\tilde{x}, \tilde{z}) = \sum_{e \in N_p} \psi_e^{\text{plate}} \quad (22)$$

2.3. Density mapping

Rather than calculating support structure directly from element centroid positions and the rotated build direction vector in Figure 4 (A) as done with overhanging area, the FE densities are mapped to a new AM density field (of length N_{AM}) belonging to a structured mesh aligned with the build direction in Figure 4 (B). A layer-by-layer approach is used, rather than a density gradient approach, as a structured mesh is needed to propagate support structure in linear columns towards the build plate. The FE mesh is rotated based on the orientation design variables as

$$\tilde{r}_e(\theta) = \tilde{R}^T r_e \quad (23)$$

where \tilde{R}^T is the transpose of the rotation matrix defined in Eq. (8) and r_e and \tilde{r}_e are the original and rotated element centroid locations, respectively. Conceptually, r_e represents the element centroid location in the FE coordinate system Figure 4 (A) and \tilde{r}_e represents the element centroid location in the AM $\tilde{x} - \tilde{y} - \tilde{z}$ coordinate system in Figure 4 (B). The rotated FE mesh is superimposed with the AM mesh, which has fixed \tilde{r}_e element centroid locations, as shown in Figure 4 (B).

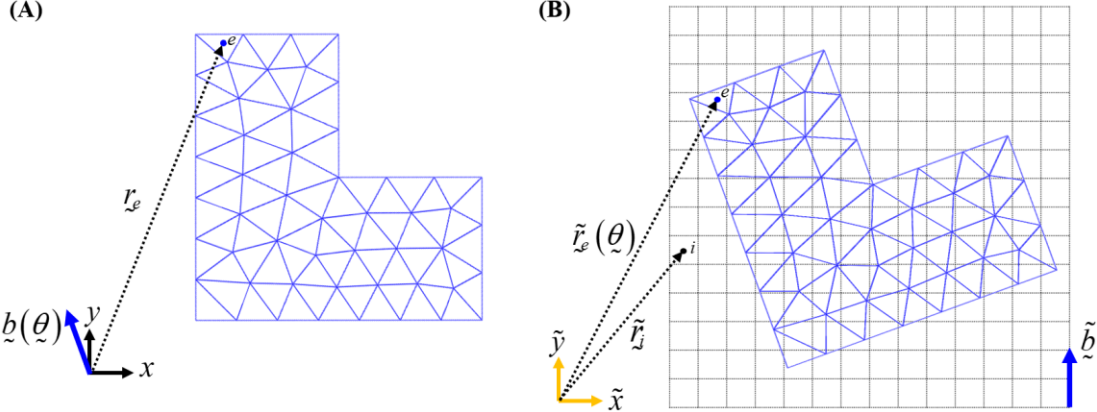


Figure 4 Mesh rotation and mapping from (A) FE mesh with rotated build direction vector to (B) AM mesh overlapping with the rotated FE mesh

The AM mesh, which is generated once at the start of the optimization, must be defined such that it covers the entire possible rotation range of the FE mesh based on Eq. (23). However, this can result in a very large AM mesh depending on the location of the FE mesh in its coordinate system. The FE mesh can be translated to the center of its coordinate system to reduce its possible rotation region and the required number of elements in the AM mesh (and ultimately computational performance).

The relative sizes of the FE and AM meshes are also important for successful density mapping because an excessively coarse AM mesh will not capture enough detail from the FE mesh, whereas an excessively fine AM mesh will result in unnecessary computational requirements. In this work, the FE mesh is scaled so that the average element length is $\bar{l}_{FE} = 1$. The average length scale of the AM mesh \bar{l}_{AM} is then defined such that the AM mesh element volume is a similar magnitude to the average FE volume. For structured hexahedral FE meshes, the AM mesh scale should not be identical to the FE mesh scale to maintain smooth differentiability (by avoiding scenarios where a uniform hexahedral FE mesh perfectly overlaps with the AM mesh at specific orientations). A recommended value for the AM mesh length scale is $\bar{l}_{AM} = \sqrt[3]{0.75\bar{v}_e}/\bar{l}_{FE}$, which results in an AM element volume that is 25% smaller than the average FE volume \bar{v}_e . For the problems in this work, this resulted in an AM mesh scale approximately equal to $\bar{l}_{AM} = 0.90$ for hexahedral meshes and $\bar{l}_{AM} = 0.45$ for tetrahedral meshes.

The transfer of density between the e -th FE and the i -th AM element is a function of the distance between the elements, as shown in Figure 5 (A) and calculated as

$$\tilde{s}_{ie}(\theta) = \tilde{r}_i - \tilde{r}_e, \quad (24)$$

$$\|\tilde{s}_{ie}(\theta)\| = \sqrt{\sum_{j=1,3} (\tilde{s}_{ie})_j^2 + \varepsilon_s}, \quad (25)$$

where the $\varepsilon_s = 0.0001$ parameter ensures a smooth magnitude calculation for near-zero \tilde{s}_{ie} vectors. A density mapping term is then calculated as

$$\gamma_{ie}(\theta) = S_R^\gamma(\|\tilde{s}_{ie}\|), \quad (26)$$

where S_R^\square is a reverse smooth Heaviside function $S_R^\square(a, \eta) \equiv S_H^\square(-a, -\eta)$ that smoothly changes from 1 to 0 at a threshold value as shown in Figure 5 (B). This results in a large γ_{ie} mapping term when the e -th FE is close to the i -th AM element and a mapping term approaching zero when these elements are far from each other.

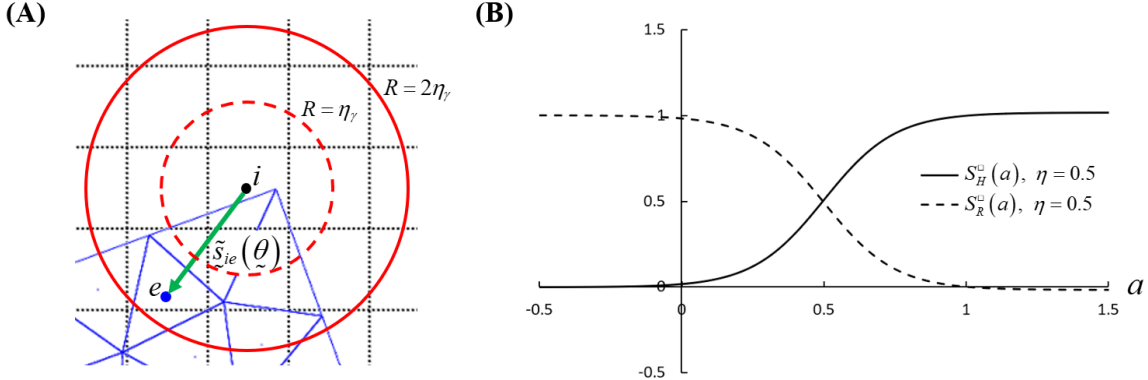


Figure 5 Calculation of the density mapping term using (A) the vector between the i -th AM element and e -th FE and (B) the reverse smooth Heaviside function

The i -th AM density is calculated through a sum of physical density, weighted by the γ_{ie} mapping terms and v_e element volumes as

$$\bar{\omega}_i(\tilde{x}, \theta) = \frac{1}{a_\omega} \sum_e \gamma_{ie} v_e \rho_e, \quad (27)$$

where a_ω is a scaling constant that ensures the resultant AM densities are scaled to values less than or equal to 1. Scaling is needed because the density mapping calculation is a function of the distance between elements rather than the overlap between elements and is therefore not inherently volume preserving. The constant is calculated as

$$a_\omega = \bar{v}_e \sum_{i \in Z} \sum_{j \in Z} \sum_{k \in Z} S_R^r \left(\sqrt{i^2 + j^2 + k^2} \right), \quad (28)$$

where \bar{v}_e is the average element volume of the FE mesh and Z is the set of all integers. This constant is calculated from the sum of density mapping terms for a single element from a cubic FE mesh perfectly overlapping with the AM mesh ($a_\omega = \bar{v}_e \sum_e \gamma_{ie}$), which represents the maximum density possibly mapped to a single AM element.

The smooth reverse Heaviside threshold limit η_γ from Eq. (26), corresponds to the radius of a circle (or sphere in 3D) around the i -th AM element, shown by the dotted line in Figure 5 (A). All e -th rotated FEs that have centroids within the radius represented by $2\eta_\gamma$ will have density mapped to the i -th AM element. The η_γ parameter affects both the smoothness of density mapping function with respect to build orientation and the similarity between the FE and AM density fields. For large threshold limits, many FEs are included in the radius and the AM density field becomes over-smoothed, while for small threshold limits, some radii may not include any FEs and the AM field becomes discontinuous. For the examples tested in this work, a threshold limit of $\eta_\gamma = 1$ (the average length scale of the scaled FE mesh) resulted in a good trade-off between these factors. Note that this larger threshold limit (and associated radius) results in some FEs contributing to AM density even if the two elements do not overlap. However, the AM densities do not overshoot a value of 1 because of the a^ω scaling factor.

Calculating all mapping terms in Eq. (26) and their derivatives requires $N_p \times N_{AM}$ and $N_p \times N_{AM} \times 2$ operations, respectively. Because the AM mesh must span the entire rotational range of the FE mesh, N_{AM} is typically an order of magnitude greater than the number of FE elements, N_p . This increased AM mesh size and the $O(n^2)$ nature of the density mapping calculation results in a large computational cost in terms of both CPU time and memory requirements. However, most weighting terms for any given orientation have near-zero values that do not meaningfully contribute to AM density. Rather than using the $S_R(a, \eta) \equiv S_H(-a, -\eta)$ reverse Heaviside function in Figure 5 (B) that has small non-zero terms when $a > 2\eta_\gamma$, the piecewise function in Eq. (29) can be used instead. This function is plotted in Figure 6

against the $S_R(a, \eta) \equiv S_H(-a, -\eta)$ function, showing that the piecewise function is equal to 0 for all elements that fall outside of the $R = 2\eta_\square$ radius depicted in Figure 5 (A). This reduces the computational growth rate of the density mapping function to $O(n)$, as the near-zero terms can instead be ignored without any sacrifices to accuracy. This adjusted density mapping function can be efficiently implemented by determining the nearest AM element for each e -th FE element and calculating all non-zero γ_{ie} weighting terms based on the structured nature of the AM mesh. Note that Eq. (29) does not have a slope parameter because the function is always continuous at its piecewise transition of $S_R^o(2\eta_\square) = 0$ and that the function is not valid for inputs less than zero. With this adjusted function, the summations in the a_ω scaling term calculated in Eq. (28) can be reduced to the set of $\{i, j, k \in Z \mid \sqrt{i^2 + j^2 + k^2} < 2\eta\}$.

$$S_R^o(a) = \begin{cases} 0, & a > 2\eta_\square \\ 2\left(\frac{a}{2\eta_\square}\right)^3 - 3\left(\frac{a}{2\eta_\square}\right)^2 + 1, & \text{otherwise} \end{cases} \approx \begin{cases} 0, & a > \eta_\square \\ 1, & a < \eta_\square \end{cases} \quad (29)$$

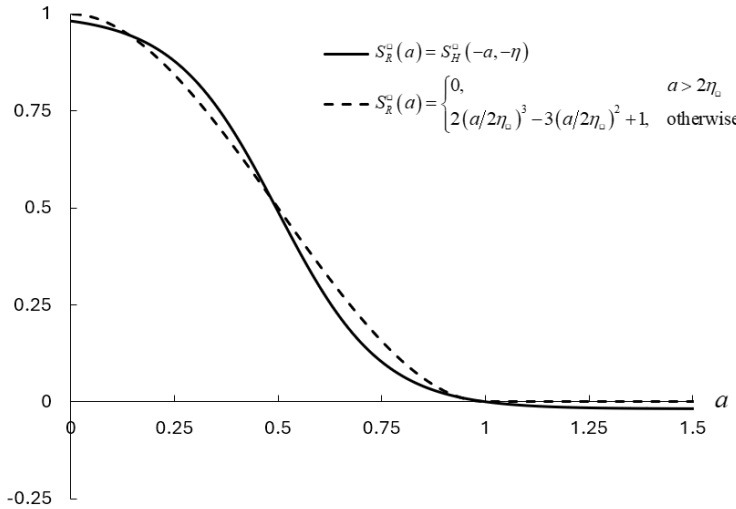


Figure 6 Piecewise reverse Heaviside function used to reduce computing time, plotted for $\eta = 0.5$

After mapping densities to the structured AM mesh, the AM element density field is filtered to improve smoothness with respect to build orientation design variables and thresholded to improve discreteness of the AM densities in Eq. (30). The weighting term \tilde{d}_{ij} is defined in Eq. (3) from the i -th element to the N_i neighbouring j -th elements within the filter radius R_F^{AM} .

$$\omega_i(x, \theta) = S_H^\omega \left(\frac{\sum_{j \in N_i} \tilde{d}_{ij} \bar{\omega}_j}{\sum_{j \in N_i} \tilde{d}_{ij}} \right) \quad (30)$$

The density mapping process is demonstrated in Figure 7 for two sample TO density fields in (A) and (B). It is apparent that the density mapping inherently smooths the element densities in Figure 7 (C) and (D), removing features that are a single element thick and blurring the exterior boundaries of the geometry. This smoothness is needed to ensure smooth differentiability and convergence behavior with respect to rotation design variables. The filtered and thresholded field has difference from Figure 7 (C) to (E), but yields improved discreteness from Figure 7 (D) to (F). A zoomed-in view of the boxed regions in Figure 7 is included in Figure 8 to show the mapping in more detail. The thinner members in Figure 8 (B) are almost removed in Figure 8 (D), but the filtering and thresholding step in Figure 8 (F) improves

discreteness to more closely match the original physical densities. It should be noted that the AM densities are asymmetric in Figure 7 (C) and (E) because the AM mesh is aligned with the build plate rather than the symmetry plane of the cantilever beam (as with the original FE mesh). It is impossible to achieve symmetry when the mesh is not aligned, but this is not expected to influence the support structure calculation because the asymmetry is minor.

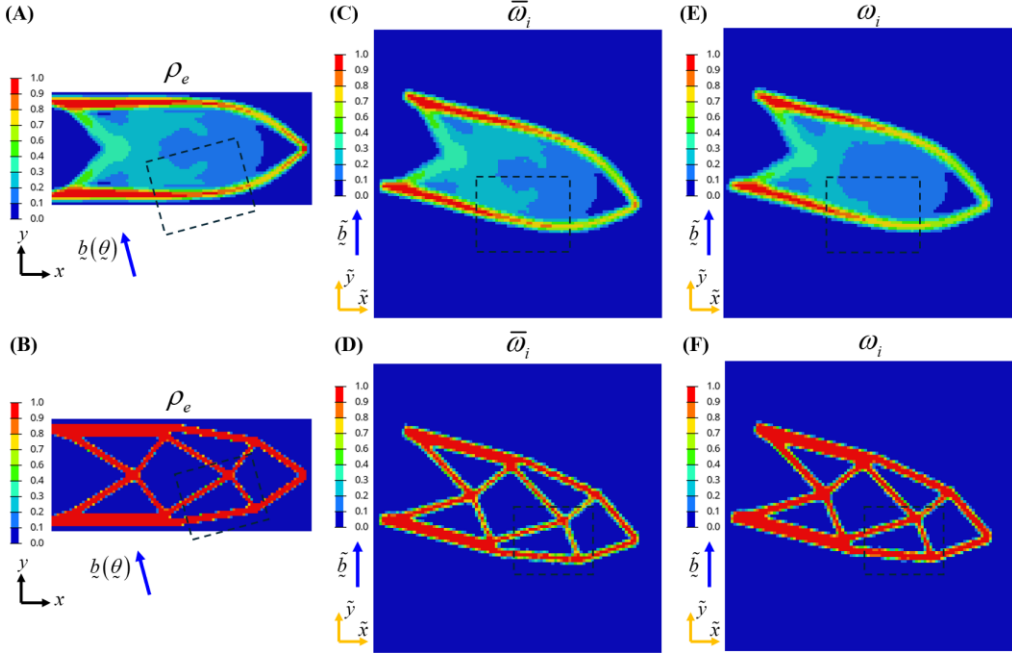


Figure 7 Density mapping process for (A) intermediate and (B) nearly discrete TO results, with (C)-(D) showing structured AM densities and (E)-(F) showing filtered and thresholded AM densities

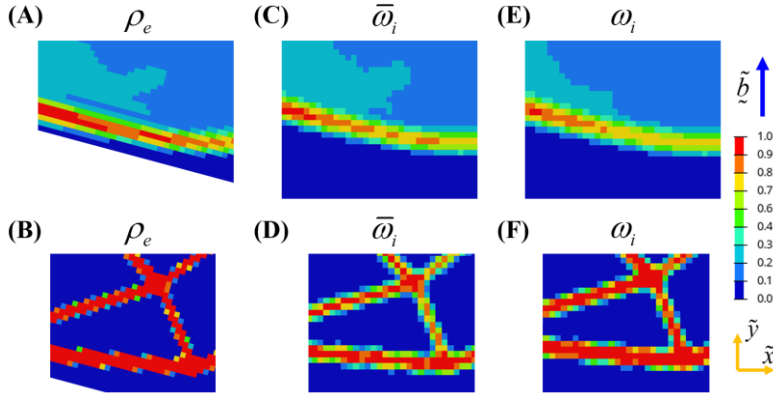


Figure 8 Close-up view of density mapping process for boxed section of Figure 7

As seen in Figure 7, at any given orientation, there will be a set of AM elements that are far from any rotated FEs and therefore have zero density. If these AM elements are below a FE, they may have support density and could be meaningful to the solution. However, if they are far from and are not below any FEs, they cannot have AM or support density and are therefore not meaningful to the support volume calculation for that orientation. In addition, elements well below the build plate are not significant and can also be ignored without compromising accuracy. These elements can therefore be ignored to reduce computational time and memory requirements, as pictured in Figure 9 for an example 2D problem. Note that an offset is needed from the boundaries of the structure (about five elements from the sides and top, and 25 elements from the bottom) to ensure that sensitivity calculations remain accurate. While these plots show a moderate reduction in the number of elements in 2D problems, a more significant reduction occurs in 3D problems, resulting in significant computational savings.

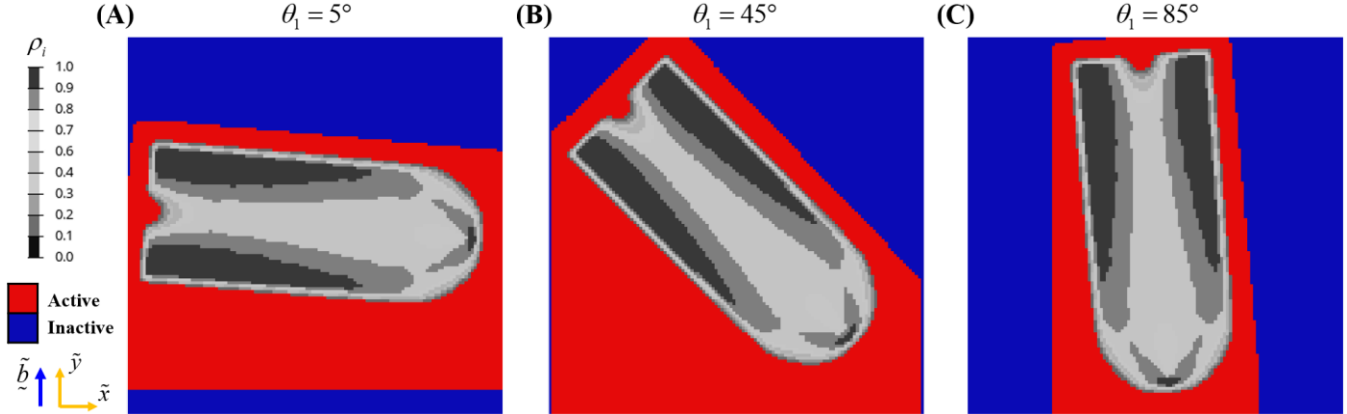


Figure 9 Inactive elements removed from support structure calculation to improve computational efficiency

2.4. Support calculation

Support structure requirements are calculated from the ω AM densities and the inherent geometric relationship between elements in a uniformly structured AM mesh. A support density field τ ranging from 0 to 1 is calculated for each element in the AM mesh, based on the supporting region N_i^S outlined in Figure 10. This supporting region, defined by Langelaar (Langelaar 2016b) includes elements within a 45° angle beneath the dark gray i -th element of interest, based on the 45° self-supporting threshold design guideline typically used for AM methods (Wang et al. 2013, Jiang et al. 2018a). A layer-based overhang calculation is used rather than the density-based approach presented in Section 2.2 because it integrates better with the layer-by-layer support structure calculation defined in the following paragraphs, and because densities are already available in a structured form through the AM mesh. Support density is needed in the k -th element if either:

1. The sum of the i -th element's AM density and support density exceeds the maximum AM density in the i -th element's supporting region ($\omega_i + \tau_i > \max(\omega_j), j \in N_i^S$); or
2. the i -th element's support density exceeds the k -th element's physical density ($\tau_i > \omega_k$).

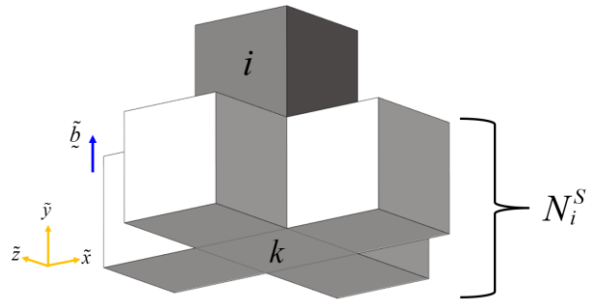


Figure 10 Supporting region for the i -th element used to calculate the k -th element's support density

The first principle ensures that a support column is initiated if the below elements within the 45° threshold cannot support the above density. The second principle ensures that a support structure column continues downwards until there is sufficient AM density to stop the support structure column. A supporting indicator ζ_i is defined to represent the level of support provided by the supporting elements, ranging from 1 for fully supported to 0 for unsupported. Eq. (31) defines the supported indicator as the smooth maximum of the physical density of the elements within the supporting region using a value of $\alpha_\zeta = 15$ for the smoothness parameter.

$$\zeta_i(x, \theta) = S_{MAX}^\zeta(\omega_j), \quad j \in N_i^S \quad (31)$$

The first and second principles are mathematically expressed through two intermediary support indicators $\bar{\tau}_k^1$ and $\bar{\tau}_k^2$ defined in Eq. (32) and (33). These indicators are greater than zero if support is needed, approach a maximum value of one for a fully unsupported element, and are less than zero if support is not needed. Note that the i and k indices refer to the upper and lower elements, respectively, depicted in Figure 10.

$$\bar{\tau}_k^1(x, \theta) = \tau_i + \omega_i - \zeta_i \quad (32)$$

$$\bar{\tau}_k^2(x, \theta) = \tau_i - \omega_k \quad (33)$$

It is important to note that Eq. (32) subtracts the supported indicator ζ_i rather than multiplying by $(1 - \zeta_i)$, which is done in other support structure approaches (Ryan and Kim 2019, Sabiston and Kim 2019, Fritz and Kim 2020, Olsen and Kim 2020) (and would result in $\bar{\tau}_k^1 = (\tau_i + \omega_i)(1 - \zeta_i)$). With a multiplication formulation, support structure could be prevented only if the supported indicator was equal to one, resulting in a $(1 - \zeta_i)$ term of zero. Instead, with the proposed subtractive approach, support can be prevented if the $\zeta_i > \omega_i + \tau_i$ condition is met, allowing for an intermediate ζ_i supporting indicator to support a smaller sum of intermediate densities $(\omega_i + \tau_i)$. The subtractive approach results in better behaviour during early TO iterations with intermediate densities but produces similar results to the multiplicative approach when element densities are discrete at the end of the optimization. This principle also applies to Eq. (33).

After calculating the two support indicators, the support structure density τ_k of the k -th element is calculated in Eq. (34) as the smooth maximum of the two support indicators, or zero if the support indicators are both negative, using a smoothness parameter of $\alpha_\tau = 15$.

$$\tau_k(x, \theta) = S_{MAX}^\tau(\bar{\tau}_k^1, \bar{\tau}_k^2, 0) = S_{MAX}^\tau(\tau_i + \omega_i - \zeta_i, \tau_i - \omega_k, 0) \quad (34)$$

It is important to note that support density τ_k must be calculated in a layer-by-layer method starting from the top layer of elements (in the print direction) and moving downwards towards the bottom of the part. This is because each subsequent k -th support indicator in Eq. (32) and (33) is a function of the support density of its above i -th element. The support density of the top layer of elements is set equal to zero as support is never needed at the top of the part. This process is summarized as follows:

1. Calculate ζ_i for all elements
2. Set $\tau_k = 0$ for the top layer of elements
3. Calculate $\bar{\tau}_k^1$, $\bar{\tau}_k^2$, and τ_k one layer at a time moving down towards the build plate

Unless interrupted by the component geometry, support density will propagate downwards in columns until reaching the bottom of the AM mesh. However, support density should stop at the build plate location, which can be calculated similarly to the method discussed in Section 2.2 and shown in Figure 3. A simplified formulation can be used here because the AM mesh is defined with positive \tilde{y} coordinates and the mesh does not rotate as a function of orientation. A new height-density term \hat{h}_k^λ is calculated in Eq. (35) based on the AM density and the \tilde{y} coordinate of the k -th element center \tilde{r}_k^2 . The bottom of the part in the AM reference frame B^λ is then calculated in Eq. (36) and the build plate indicator is calculated in Eq. (37). Note that the build plate indicator field must be calculated when printing on both a raft or the build plate, and the threshold parameter of η_μ^λ indicates the number of raft layers in the AM coordinate system ($\alpha_\mu^\lambda = 0$ for build plate and $\alpha_\mu^\lambda < 0$ for raft).

$$\hat{h}_k^\lambda(x, \theta) = \tilde{r}_k^2 S_H^{h^\lambda}(\omega_k) \quad (35)$$

$$B^\lambda(x, \theta) = S_{MIN}^\lambda(\hat{h}^\lambda) \quad (36)$$

$$\mu_k^\lambda(x, \theta) = S_H^{\mu^\lambda}(\tilde{r}_k^2 - B^\lambda) \quad (37)$$

The support structure volume for each element is then calculated by multiplying the support density, build plate indicator, and AM element volume v_k in Eq. (38), with the build plate indicator eliminating support volume in elements below the build plate.

$$\lambda_k = \tau_k v_k \mu_k^\lambda \quad (38)$$

Finally, the total support structure volume for the component can be calculated by summing support structure volume for all AM elements as follows:

$$\Lambda(x, \theta) = \sum_{k \in N_{AM}} \lambda_k \quad (39)$$

The support structure calculation is depicted for a sample AM density field in Figure 11. The two support indicator fields in Figure 11 (B) and (C) are greater than zero if support is needed and less than zero if support is not needed. Support structure density in Figure 11 (D) combines these two fields. The fields in Figure 11 (B), (C), and (D) are calculated one layer at a time from the top to bottom of the AM mesh. Support structure density is multiplied by the build plate indicator in Figure 11 (E) to yield the support volume field in Figure 11 (F), which is summed to calculate the total support structure objective. Note that the support density field in Figure 11 (D) has some small negative values because of the smooth maximum function in Eq. (34), which outputs a small negative value when both support indicators ($\bar{\tau}_k^1$ and $\bar{\tau}_k^2$) are negative and near-zero. These negative support indicators can cascade through the column of support densities, resulting in small, non-zero, negative values. These negative support densities are essentially equal to zero and are only negative due to the smoothness of the calculation, which is needed for gradient-based optimization. The small negative values also occur in support structure volume in Figure 11 (F), but do not have a significant contribution to the overall support objective.

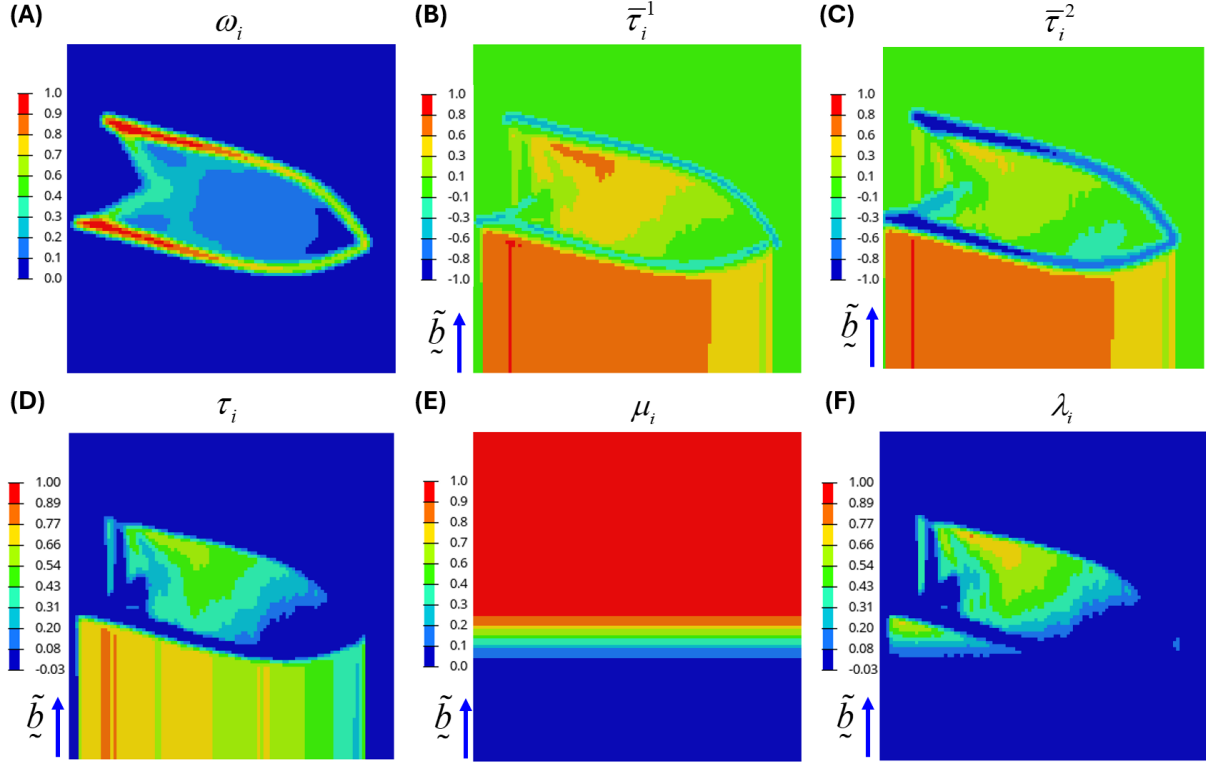


Figure 11 Support structure calculation for a sample TO result: (A) AM density, (B) support indicator 1, (C) support indicator 2, (D) support density, (E) build plate indicator, and (F) support structure volume

The smoothness of the support structure and density mapping calculation is demonstrated in Figure 12 by plotting support structure volume as a function of build orientation for a sample 2D cantilever beam problem (also shown in Figure 7 and Figure 11). Support structure volume is a smooth and continuous function of build orientation at both early and late iterations within the optimization, indicating the approach can be used for gradient-based optimization.

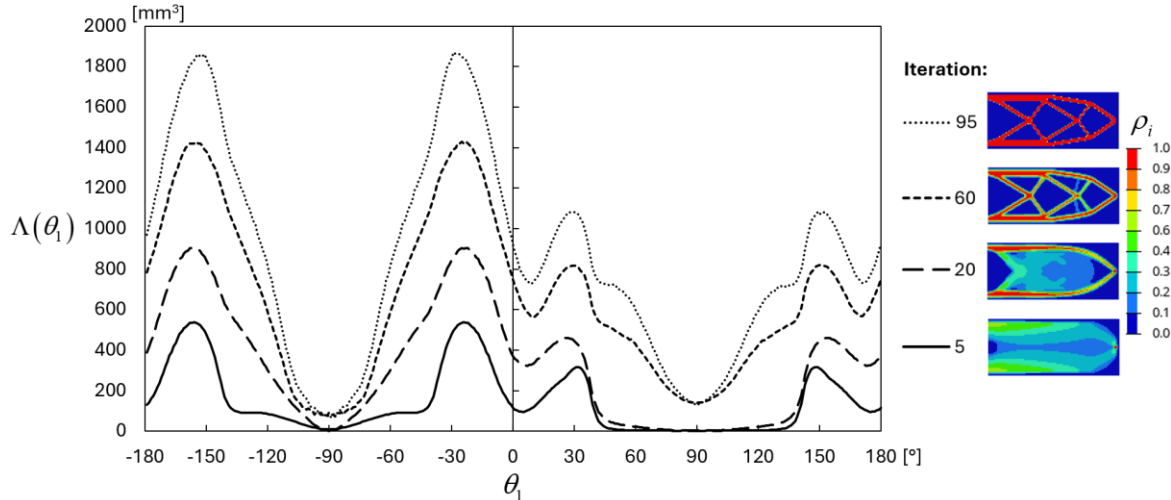


Figure 12 Plot of support structure volume as a function of build orientation for a sample 2D TO problem at select iterations

The sensitivity expressions needed for gradient-based optimization are derived and verified using the finite difference method in Appendix A.

2.5. Supporting regions for alternative self-supporting angles

The supporting region defined in Figure 10 is formulated specifically for problems with an $\bar{\alpha} = 45^\circ$ self-supporting angle due to the structured nature of the AM mesh. However, the printable overhang angle can vary depending on the AM method and the process parameters used (Wang et al. 2013, Mertens et al. 2014, Jiang et al. 2018a). With this method, the self-supporting angle can be adjusted by changing the aspect ratio of the AM mesh. Altering the element length scale in the \tilde{x} and \tilde{z} directions according to $l_{\tilde{x},\tilde{z}} = 1/\tan \bar{\alpha}$, while keeping the \tilde{y} length scale fixed at $l_{\tilde{y}} = 1$ results in a new self-supporting angle of $\bar{\alpha}$. This is demonstrated in Figure 13 for three self-supporting threshold angles, with the bottom 2D cross-section views included to visualize the self-supporting angle. Note that all density mapping and support structure calculations remain identical, and the desired self-supporting threshold can be obtained by adjusting the aspect ratio during the initial AM mesh generation.

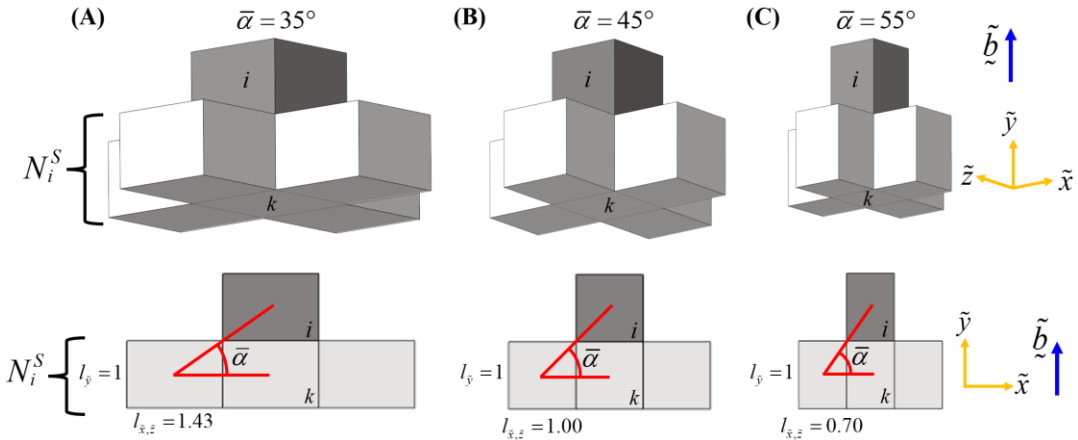


Figure 13 Adjustment of AM mesh aspect ratio to achieve alternate self-supporting threshold angles

Small or large self-supporting angles require significant changes to the aspect ratio in the AM mesh, resulting in poor mapping from FE to AM densities and inaccurate overhang identification. A very large $l_{\tilde{x},\tilde{z}}$ length scale results in an overly coarse AM mesh as shown in Figure 14 (A) with the boxed region highlighting two members that become discontinuous after translation due to the aspect ratio of the AM mesh. These features have an angle well above the self-supporting threshold but are identified as requiring support (which is plotted in shades of red) due to the discontinuities. A very small length scale accurately captures the geometry but may incorrectly evaluate overhangs. This is shown in Figure 14 (C), with the boxed region showing a surface with an angle well below the self-supporting threshold that was identified as requiring intermediate density supports. Here, the aspect ratio of the AM mesh results in alternating columns of high and low support density, as some elements on the surface partially meet the requirements of the supporting region.

To effectively consider small or large self-supporting threshold angles, alternate supporting regions are defined in Figure 15. A new supporting indicator function is also defined in Eq. (40), and an adjusted AM length scale is calculated in Eq. (41). For self-supporting angles of $\bar{\alpha} \leq 30^\circ$, the N_i^S supporting region is extended in Figure 15 (A) to include additional elements. In this case, no modifications to the supporting indicator calculation are needed. The $l_{\tilde{x},\tilde{z}}$ length scale is halved to provide a more uniform AM mesh and better capture the FE densities as shown in Figure 14 (B). For self-supporting angles of $\bar{\alpha} \geq 60^\circ$, two layers of elements are included below the i -th element in each m -th supporting region $N_i^{S,m}$ pictured in Figure 15 (C). An intermediate supporting indicator $\bar{\zeta}_m$ is calculated with the smooth minimum function in Eq. (42). For the i -th element to be solid, either the k -th element must be solid or both elements in any m -th supporting region must be solid. The $l_{\tilde{x},\tilde{z}}$ length scale is doubled with this adjusted formulation to achieve a more uniform AM mesh aspect ratio, allowing for a more accurate evaluation of support structure as demonstrated in Figure 14 (D).

$$\zeta_i(x, \theta) = \begin{cases} S_{MAX}^{\zeta}(\omega_k, \bar{\zeta}_j), & \bar{\alpha} \geq 60^\circ \\ S_{MAX}^{\zeta}(\omega_j)_{j \in N_i^S}, & \text{otherwise} \end{cases} \quad (40)$$

$$l_{\tilde{x}, \tilde{z}} = \begin{cases} 2/\tan \bar{\alpha}, & \bar{\alpha} \geq 60^\circ \\ 1/2 \tan \bar{\alpha}, & \bar{\alpha} \leq 30^\circ \\ 1/\tan \bar{\alpha}, & \text{otherwise} \end{cases} \quad (41)$$

$$\bar{\zeta}_i^m(x, \theta) = S_{MIN}^{\bar{\zeta}}(\omega_j), \quad j \in N_i^{S,m} \quad (42)$$

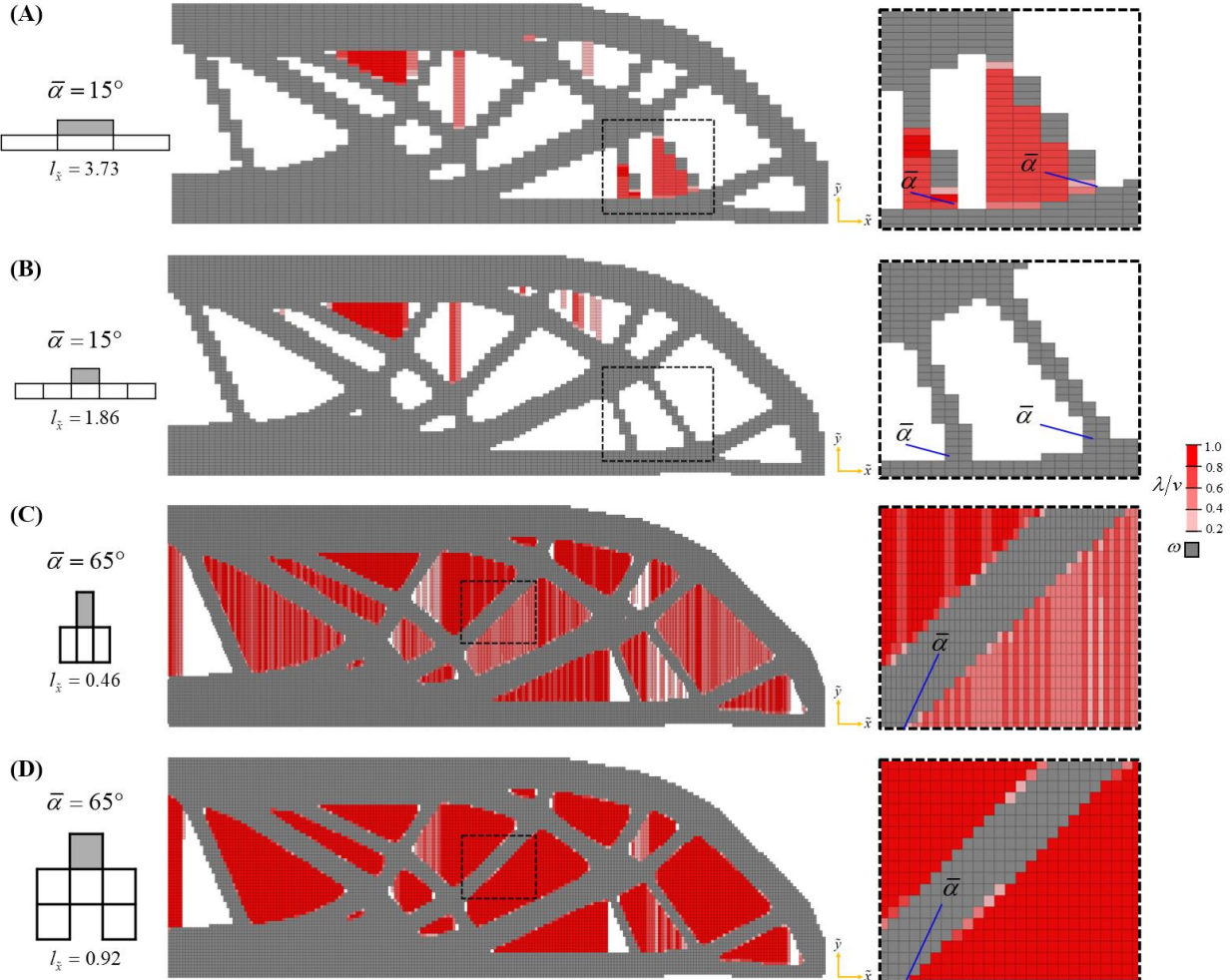


Figure 14 Support structure calculation on a sample TO result with (A) a low self-supporting threshold, (B) a low self-supporting threshold with an alternate supporting region, (C) a high self-supporting threshold, and (D) a high self-supporting with an alternate supporting region

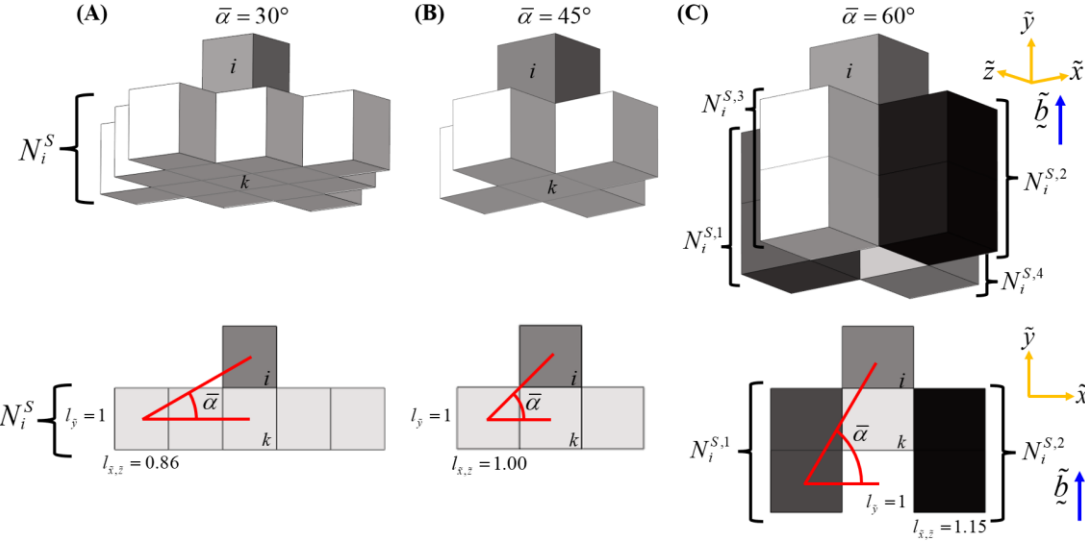


Figure 15 Alternative supporting regions for (A) small and (C) large self-supporting threshold angles

2.6. Extended supporting region for prevention of icicle structures

Icicle structures can occur when minimizing, constraining, or eliminating support structure or overhangs, as discussed in literature (also known as the dripping effect, hanging features, or boundary oscillation) (Allaire et al. 2017, Mezzadri and Qian 2020, Garaigordobil et al. 2021). These features allow the optimizer to reduce large overhanging surfaces to many small overhanging points that require only thin columns of support structure. Icicle structures can be discouraged during optimization by modifying the original supporting region from Figure 10 to include more elements along the self-supporting diagonals as shown in Figure 16. These diagonals can be extended by any number of elements or can be set equal to the original formulation without any additional elements. With this extended supporting region, the i -th element is considered fully supported only if the k -th element or an entire set of $N_i^{S,m}$ elements is solid. For the original supporting region defined in Figure 10, with one element along each diagonal ($|N_i^{S,m}|=1$), an icicle feature requires a single support structure column at the bottom “tip” of the icicle. Extending the supporting region along the diagonals by one element ($|N_i^{S,m}|=2$) results in four additional columns of support structure needed to support the icicle feature, heavily discouraging them from forming. In this work, the supporting region is extended by three elements in the first phase and reduced by one element each phase, ultimately converging to the original formulation from Figure 10.

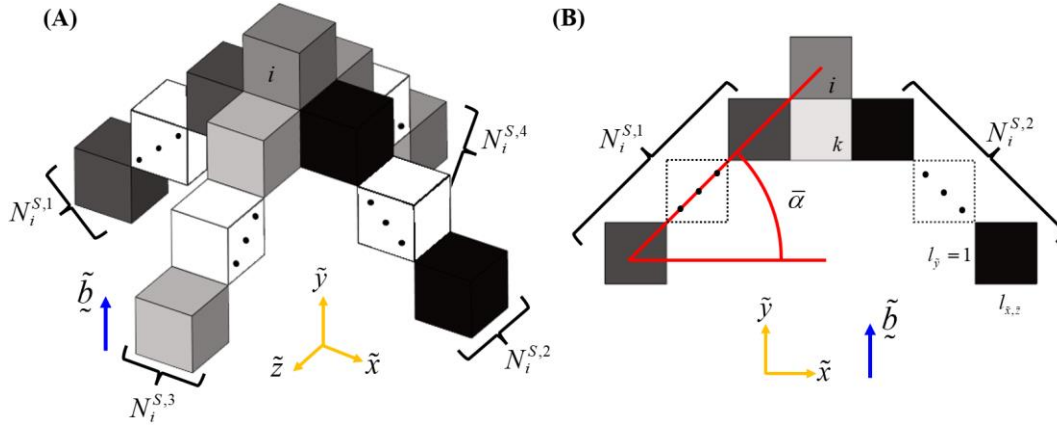


Figure 16 Alternate definition of the i -th element's supporting region to reduce the icicle effect

The supporting region extension uses the supporting indicator calculation in Eq. (40) with the $\bar{\alpha} \geq 60^\circ$ case. The intermediate supporting indicator is calculated in Eq. (42), using the $N_i^{S,m}$ supporting regions from Figure 16 rather than Figure 15 (C).

It should be noted that the goal of the extended supporting region is to discourage icicle structures from forming during optimization, not to more accurately access if a given element is printable over the extended supporting region. This is why the supporting region is extended only along the diagonals, rather than including the entire range of elements within a cone, such as in the approach from Gaynor and Guest (Gaynor and Guest 2016). Their work required the average density within the cone to be above a threshold value, which does not require each layer within the supporting region to contain density that supports the subsequent layer. Formulating an extended support region that more accurately represents printability would require a more complex supporting region definition and is left to future work. The proposed approach converges to the original (and more accurate) supporting region in the final phase of the optimization, as the additional diagonal elements are removed from the supporting region.

3. Numerical results

The proposed methodology was verified using the test problems shown in Figure 17, with a material stiffness of $E_0 = 70$ GPa and a load of 1000N applied at a point in (A), over a 20×40 mm area in (B), and over a 100×100 mm area in (C). The 2D MBB beam in Figure 17 (A) is identical to the geometry defined by Langelaar (Langelaar 2017) and is used to compare the approach to existing literature. The airplane bearing bracket in Figure 17 (D) is from an online design challenge (GrabCAD 2016) and was meshed using 226k unstructured tetrahedral elements, representing a real-world application. Loads were applied to a node in the center of the bearing interface connected using an RBE2 element, with a magnitude of 5560 N, 11120 N, and 8340 N (1250, 2500, and 1875 lbf), applied in the x , y , and diagonal directions as indicated. Single point constraints were applied to the center of the four mounting holes using RBE2 elements. The compliance of the solid design space for the four problems were 762 mJ, 0.550 mJ, 1.042 mJ, and 20.56 J (summed over all load steps), respectively. The addition of a layer of void elements in the domain extension approach (Clausen and Andreassen 2017) resulted in a total of about 11.6k elements for (A), 273k elements for (B), 201k elements for (C), and 275k elements for (D). The length scale of the AM mesh was set to $\bar{l}_{AM} = 0.90$ for the MBB beams and box, and $\bar{l}_{AM} = 0.45$ for the airplane bracket as it was meshed with tetrahedral elements. Note that the symmetry constraint in the MBB beam problems was used only for structural analysis, while support structure was calculated only for the half-MBB beam.

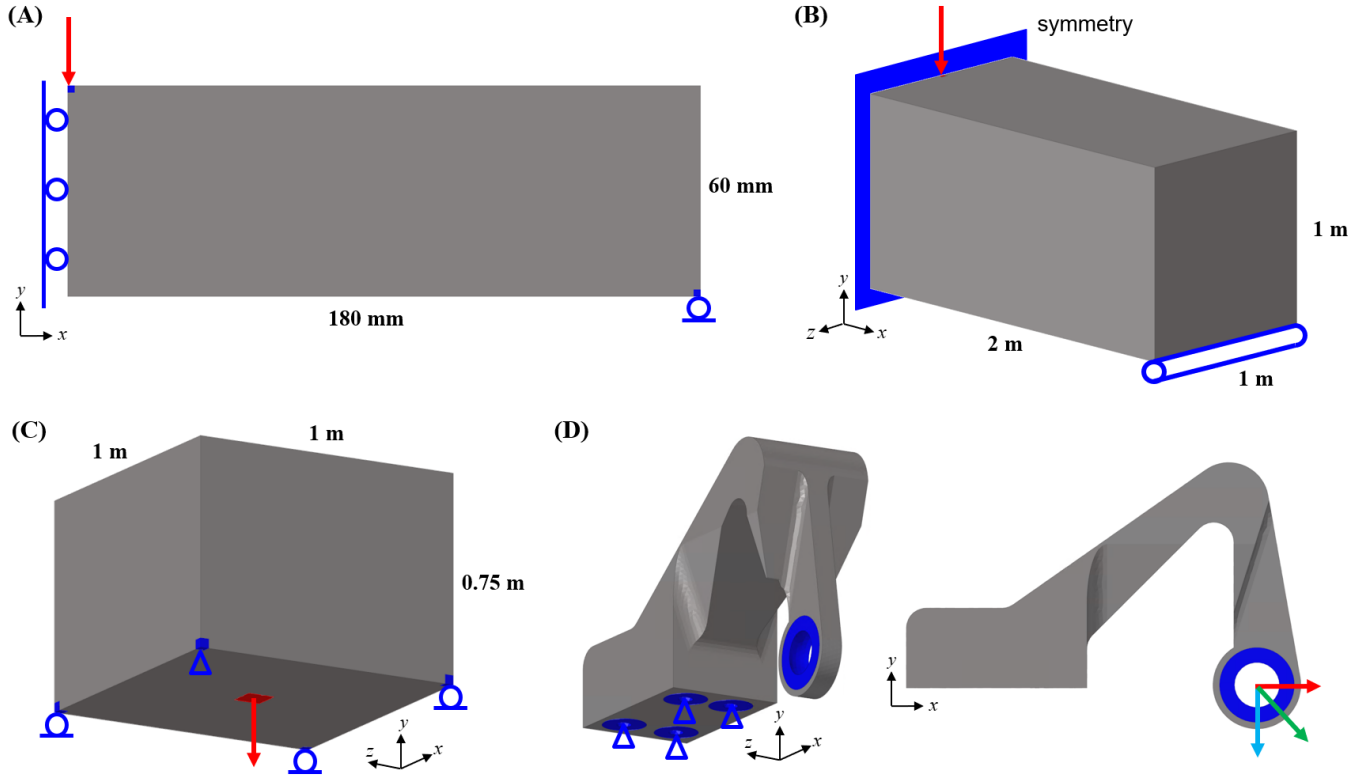


Figure 17 Numerical test problems including A) 2D MBB beam with 180×60 elements, B) 3D MBB beam with $250 \times 100 \times 100$ elements, C) simply supported box with $60 \times 45 \times 60$ elements and D) Airplane bearing bracket (GrabCAD 2016)

The problem statement from Eq. (1) was solved using Altair OptiStruct (Inc. 2023) for FE analysis and the Method of Moving Asymptotes (MMA) (Svanberg 1987) for gradient-based optimization. A four-phase continuation scheme was used, with increasing SIMP penalty function and Heaviside smoothness parameter values after objective function convergence within 0.5% over the last two iterations. Fixed parameter values were used for the smooth maximum/minimum functions. A filter radius of $2 \times$ the average element size and a self-supporting threshold of $\bar{\alpha} = 45^\circ$ were used for each problem, unless otherwise noted. The interface radius for overhang area calculation was initialized at $5 \times$ the average element size and decreased by $1 \times$ each phase to prevent boundary oscillations (Garaigordobil et al. 2021). The standard supporting region from Figure 10 was used for all problems except for the 2D MBB beam, which used the supporting region in Figure 16, starting with three added diagonal elements and reducing by one each phase. Detailed parameter function values are provided in Table B.1 in Appendix B.

Element density design variables were initialized at the volume fraction constraint limit, and build orientation was initialized both manually and with an automatic approach (Crispo and Kim 2024a), as specified in each section. The automatic build orientation initialization performs standard TO for 5 iterations, searches the orientation design space in coarse intervals ($\Delta = 45^\circ$), then begins topology and build orientation optimization from the orientation that results in the lowest AM cost objectives. Objective functions were normalized with the compliance of the initial iteration $C_0 = C(\underline{x}_0)$, the volume of the design space $\Lambda_0 = V(\rho=1)$ and the surface area of the design space $\Psi_0 = \sum_{e \in N_p} \phi_e(\rho=1)$. The selected objective function weighting factor values are discussed in each section. Final physical densities were thresholded and objective function values were recalculated with nearly discrete smoothness parameters to ensure fair comparison between designs and to facilitate comparison across literature (Sigmund 2022). Note that while the thresholded physical densities are discrete, the AM densities are not discrete in the final calculation due to the smooth density mapping function.

3.1. Topology optimization for support structure volume

The proposed support structure minimization TO approach was compared to a self-supporting method from literature using the 2D MBB beam problem (Langelaar 2017). The AM cost weighting factors were set to $q_\Lambda = 1$ and $q_\psi = 0$, and the optimization was performed for a sweep of w weighting factors without build orientation design variables. The number of elements, filter radius, and volume fraction match those defined by Langelaar and all numerical values are compared relative to the respective baseline designs. Results are compared in Figure 18 for two print directions, labelled as north and south, with a 0.2 iso filter of AM density plotted in black, and volume-normalized support structure density plotted in red. The support structure field is continuous, as with element density, but in this case full density supports correspond to overhangs well above the self-supporting threshold, intermediate density supports occur for surfaces with an angle close to the self-supporting threshold, and low-density supports are used for surfaces approaching the threshold angle. Support structures are plotted with different shades of red to visualize this behaviour and to identify intermediate density supports that may not be needed or could be potentially eliminated with small changes to the geometry.

The approach from Langelaar uses a TO problem statement of minimizing compliance with a volume fraction constraint and applies a projection technique named an “AM filter” that excludes unprintable element densities from the physical density field based on a supporting region similar to Figure 10. Therefore, the AM filter produces only two points on the graph in Figure 18 for each orientation, the self-supporting design and the baseline design (at point 1, 1). The AM filter from Langelaar produced self-supporting designs with 6% and 11% increases in compliance, depending on the print orientation. While the proposed approach cannot guarantee a self-supporting design, performance similar to the Langelaar solutions was achieved when a high weighting was placed on the support structure objective. For example, the $w=0.6$ solution in the south print direction reduced support volume by 92% with a 5% increase in compliance, which is significantly improved over existing support minimization approaches summarized in Table 1. The resultant structures for high support structure weightings are also visually similar to the self-supported designs from Langelaar. In some cases, the proposed method identified support requirements for features that are not identified as requiring support in the Langelaar filter, such as at the intersection between two self-supporting surfaces, circled in blue in the $w=0.6$ result. These regions could be altered in a post processing step to meet self-supporting requirements with minor adjustments. An advantage of the presented approach is that it can also produce a range of designs with smaller increases in compliance, such as the $w=0.9$ solution in the north print direction. This result reduced support structure by 53% with only a 2% increase in compliance, which may be more desirable when compared to the self-supporting design with an 11% increase in compliance.

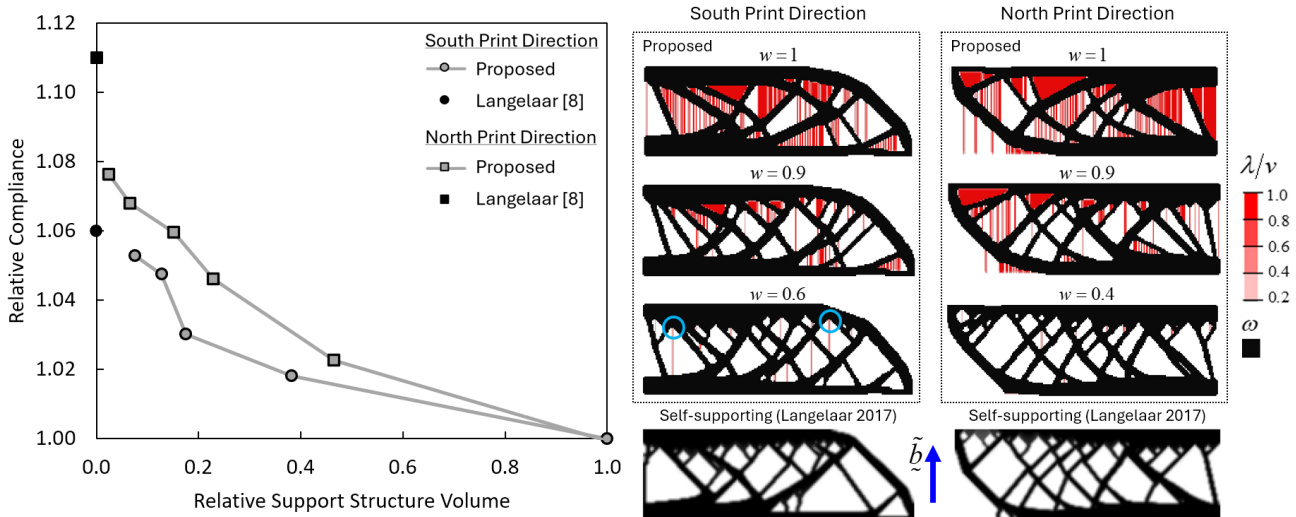


Figure 18 Comparison of the proposed support structure volume method to Langelaar self-supporting approach (Langelaar 2017)

The 3D MBB beam problem was solved with three volume fraction constraints with weighting factors of $w=1.00$, $w=0.98$, and $w=0.50$. Results are summarized in Figure 19 for a fixed print orientation of $\theta=(0^\circ, 0^\circ)$ when printing on the build plate, with final objective function values normalized across each row of equivalent volume fraction. Intermediate support structure density seen in light red occurs for surface angles close to or at the self-supporting threshold angle. For the MBB beam in this orientation, nearly all support structure was removed without increasing compliance. This is possible because there are several local minima TO solutions with similar compliance that have varying levels of support structure. A local minimum that reduces support structure was achieved by including support structure volume in the multi-objective framework. This behaviour was also discussed by Langelaar (Langelaar 2016b), however it was found that achieving self-supporting designs with equivalent compliance is possible in only select orientations. It should also be noted that the proposed approach does not consider the accessibility to remove support structure within internal voids, which occur in the result in Figure 19 (G). In this case, internal supports were removed through support structure minimization in Figure 19 (I), however these internal supports should be eliminated (rather than minimized) from any optimized design. This could be integrated into the optimization in future work using an approach similar to methods presented in literature (Sabiston and Kim 2020, Wang 2022, Wang et al. 2024).

Support structure volume was minimized for other fixed orientations with a 15% volume fraction constraint in Figure 20, with results normalized relative to Figure 19 (A). A change in orientation for the baseline design in Figure 20 (A) – (E) resulted in up to a 16 \times difference in support structure requirements. A weighting factor of $w=0.5$ in Figure 20 (K) – (O) resulted in a 90% or greater reduction in support structure volume for each orientation, respectively. However, the associated increase in compliance varied significantly, with the $\theta=(45^\circ, 45^\circ)$ orientation in Figure 20 (O) resulting in a 24% increase in compliance. If this increase is undesirable, the multi-objective solution also produces a range of designs, such as in Figure 20 (J), where support volume was reduced by 20% with an equivalent compliance to the baseline result.

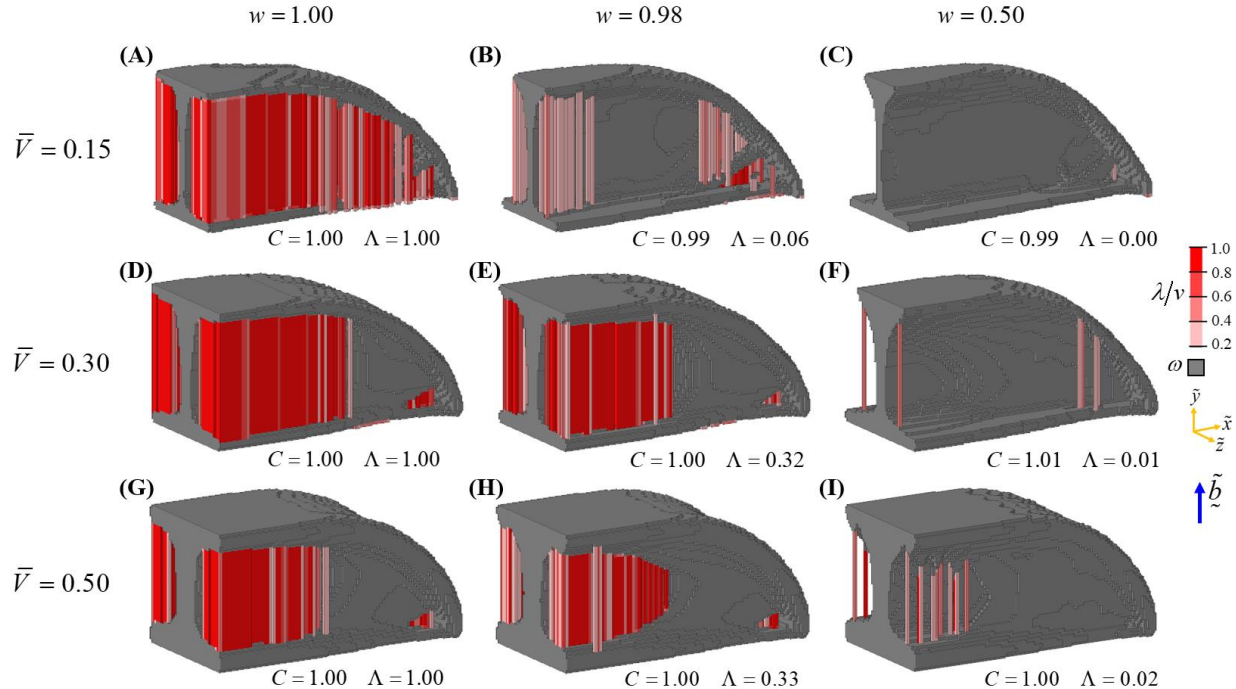


Figure 19 Support structure volume minimization with various volume fraction constraints for the 3D MBB beam problem with a fixed $+y$ build orientation

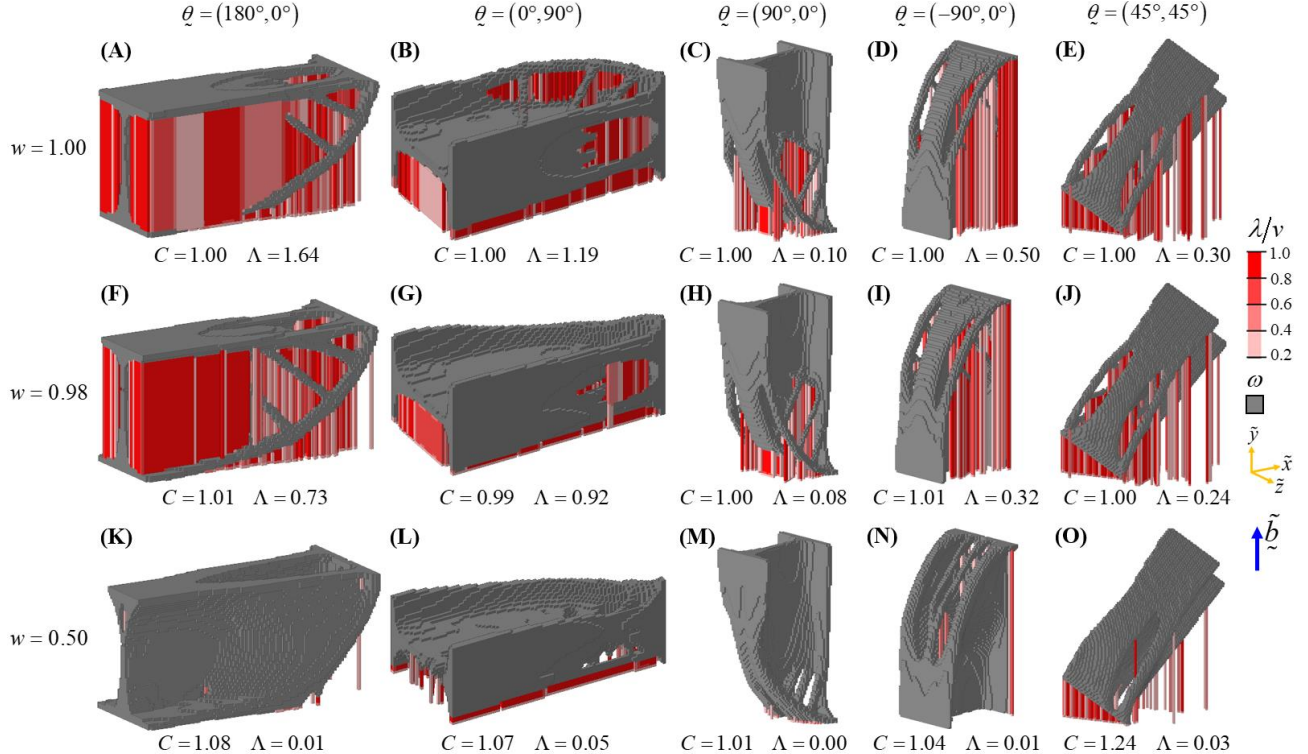


Figure 20 support structure volume minimization for the 3D MBB beam problem with $\bar{V} = 0.15$ and various fixed build orientations

The results from Figure 19 (I) and Figure 20 (L) had icicles structures, which can be reduced (or in some cases eliminated) by using the extended supporting region presented in Figure 16 and the continuation scheme discussed in Section 3. Optimization results with the extended supporting region are compared to the original formulation in Figure 21, achieving similar performance with no or reduced icicle structures in (B) and (D), respectively.

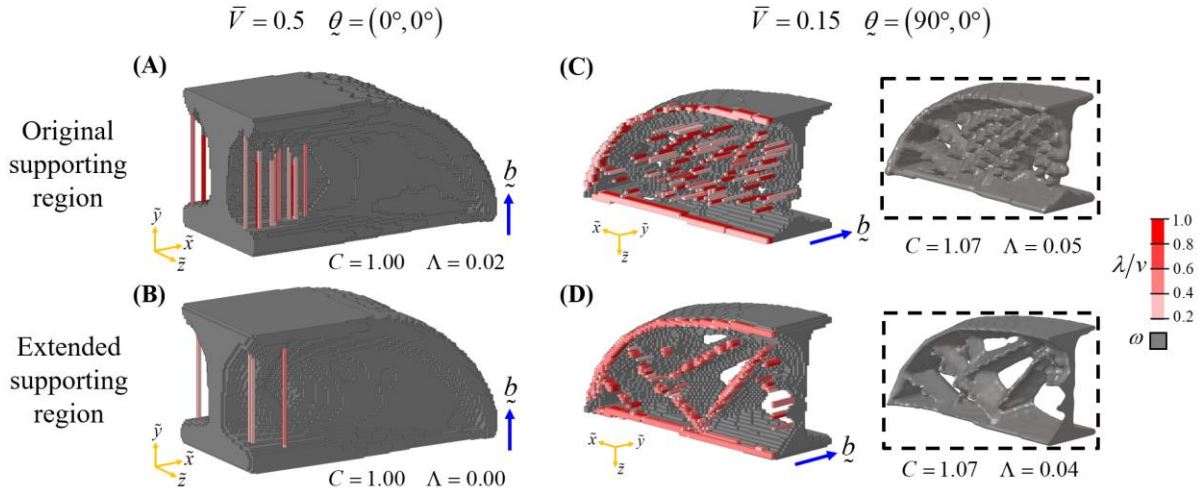


Figure 21 Extended supporting region used to (A)-(B) eliminate icicle structures or (C)-(D) reduce icicle structures with dashed boxes showing a smooth iso-filer of physical density

The optimizations from Figure 20 (A) and (K), with an orientation of $\theta = (180^\circ, 0^\circ)$ and a volume fraction constraint of $\bar{V} = 0.15$, were repeated for self supporting threshold angles between $\bar{\alpha} = 25^\circ$ and $\bar{\alpha} = 65^\circ$, using the alternative

supporting regions defined in Figure 13 and Figure 15. The results in Figure 22 (A) – (E) show that for the baseline TO result (i.e. only considering compliance), support structure volume increased/decreased with increasing/decreasing self supporting thresholds as expected. When minimizing support structure in Figure 22 (F) – (J), compliance increased slightly with self-supporting angle, as the steeper angle imposes harsher design restrictions to avoid support structure. A smooth iso filter of physical density along the symmetry plane of the MBB beam is shown in the dashed boxes alongside the self-supporting angle, demonstrating that the proposed approach effectively produces designs that meet the self-supporting threshold. Support structure was not eliminated in Figure 22 (I) and (J), but a reduction in the w weighting factor would further decrease support structure volume, albeit with a larger increase in compliance.

Objective and constraint function history is shown in Figure 23 for two results from Figure 20 (A) and (K), with vertical grey lines representing the convergence of each phase. Function values are normalized relative to the maximum value of each response in Figure 23 (A). A contour plot of normalized support structure volume and AM density is included at select iterations with a 0.1 iso filter. History in Figure 23 (A) with zero AM cost weighting ($w=1.00$) shows support structure volume calculation throughout the optimization. Support structure volume was initially near zero and gradually increased as the structure became more discrete, with abrupt jumps at the start of each phase as parameter values are increased. Support structure volume was negative in early iterations because of an accumulation of small negative values across many elements, when no “real” support structure was required in the component. This is discussed in Section 2.4 in more detail and is conceptually equivalent to zero support structure volume. The support structure volume in Figure 23 (B) was near zero throughout the entire optimization as the approach effectively eliminated support structure in this orientation.

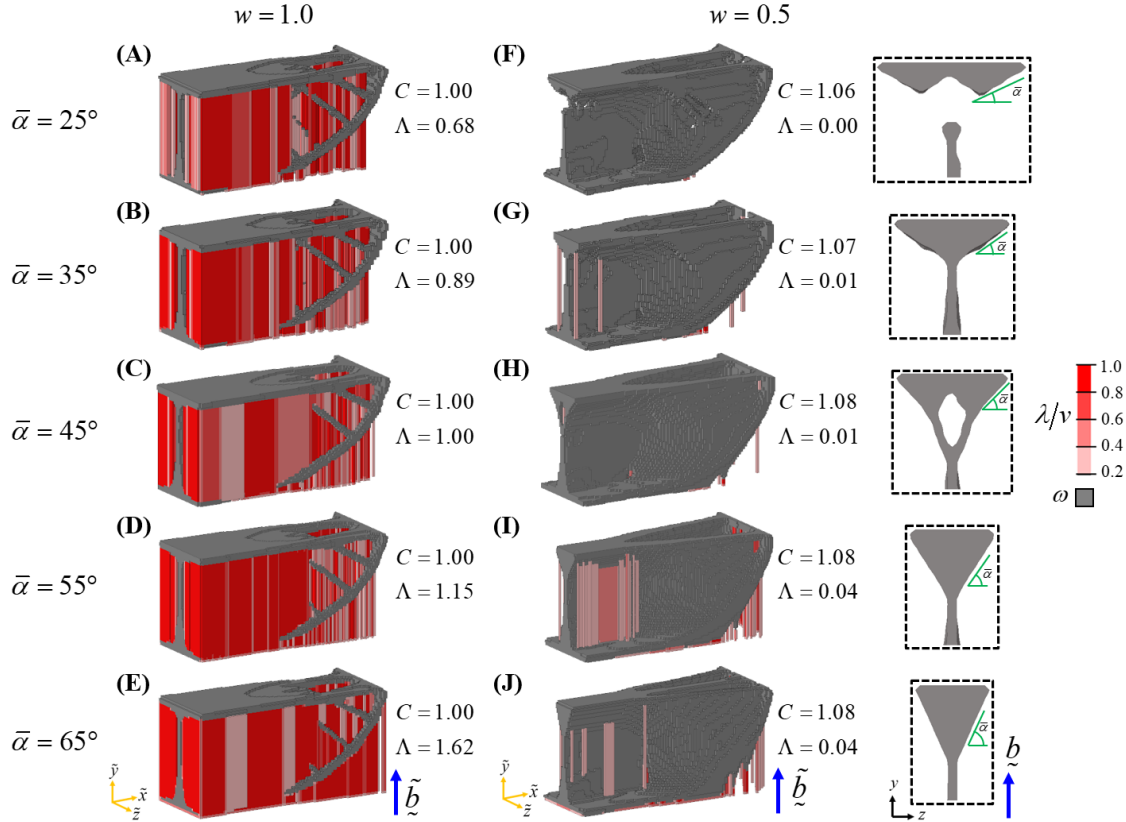


Figure 22 Effect of self-supporting threshold angle on support calculation and optimized design, with dashed boxes showing a cross-section of the end face of the beam

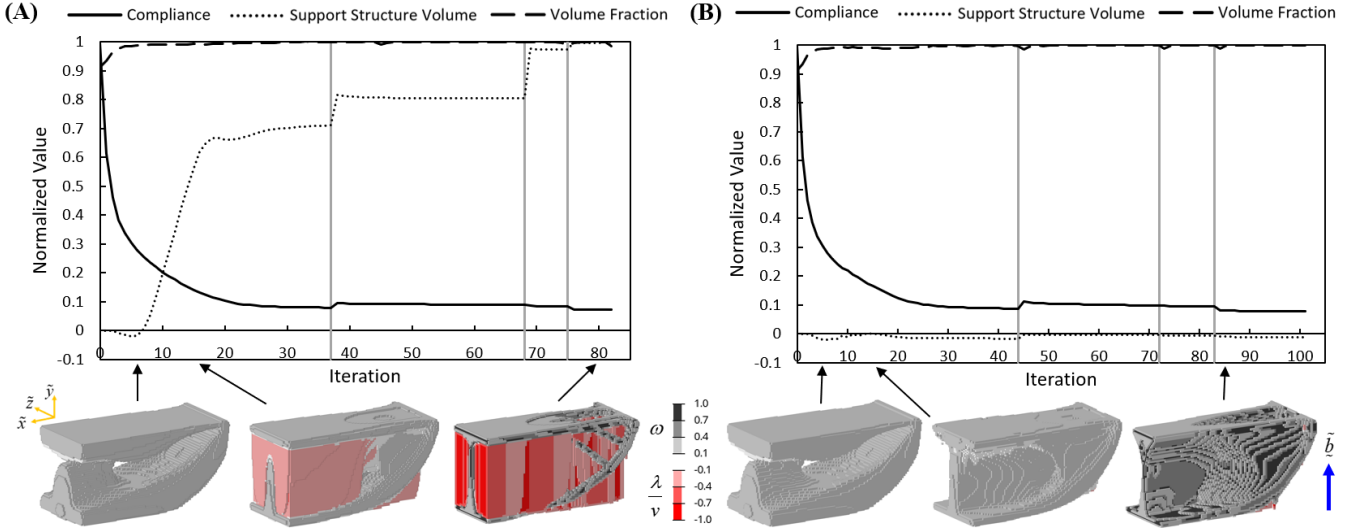


Figure 23 Convergence history and support/density contour plots for the $\theta = (180^\circ, 0^\circ)$ results for (A) $w=1.00$ and (B) $w=0.50$ from Figure 20

3.2. Topology and build orientation optimization for support structure volume

Build orientation optimization was added to the TO problem statement, which was solved using a 15% volume fraction constraint and weighting factors of $w=0.5$ and $q_\lambda=1$ to consider compliance and support structure volume ($q_\psi=0$). Build orientation design variables were initialized at five different vectors pointing along the principal axes. The optimization was completed using both build plate ($\eta_\mu^\lambda=0$) and raft ($\eta_\mu^\lambda=-5$) support structure calculations. Results are summarized in Figure 24, with objective function values normalized across each row. When printing on the build plate in Figure 24 (A)-(E), each initial orientation resulted in convergence to a different final orientation. While there are large differences in support volume between results, it is important to note that all designs had significant reductions in support structure volume (94 – 99%) relative to the original baseline TO result from Figure 19 (A). The $\theta=(0^\circ, 90^\circ)$ initialization in Figure 24 (E) converged to a poor local minimum orientation, resulting in the optimizer making significant structural changes to reduce support structure volume. It is also of note that the best initializations in Figure 24 (A) and (B) had equivalent compliance and support volume despite large differences in topology and orientation, indicating the presence of several equivalent local minima. The results with an orientation marked by an asterisk converged to an orientation outside of the limits defined in the problem statement and were translated to an equivalent orientation within the feasible design variable bounds.

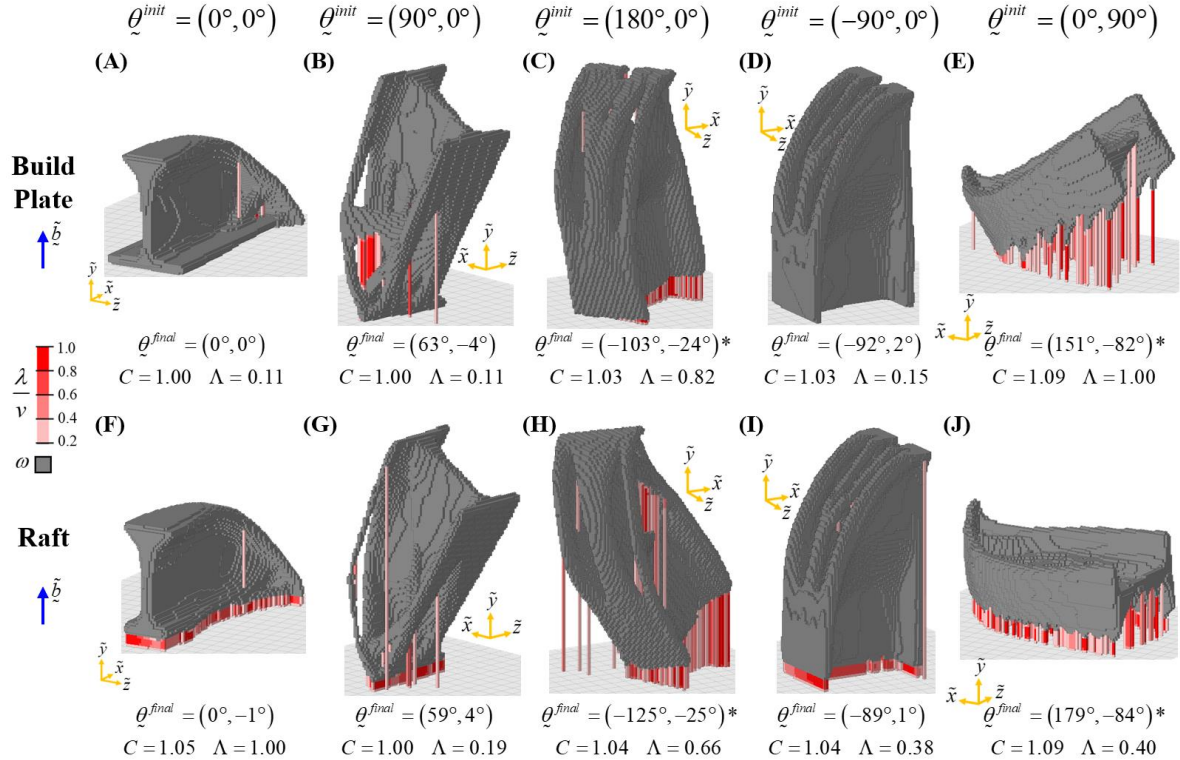


Figure 24 Simultaneous topology and build orientation optimization comparing five manual orientation initializations and the automatic initialization method for printing on (A)-(F) the build plate and (G)-(L) a raft

The optimization results when printing on a raft in Figure 24 (F) – (J) also converged to a unique orientation for each initialization, with (G) achieving the best solution. Less support structure volume reduction was achieved when printing on a raft (compared to the build plate), as support structure is always needed on the bottom face. In this case, there was a clear optimal orientation when printing on a raft in Figure 24 (G), whereas there were multiple nearly equivalent orientations when printing on the build plate (Figure 24 (A), (B), (D)). The importance of differentiating between a build plate and raft AM method is evident from the $\theta = (0^\circ, 0^\circ)$ initialization, which produced the best design when printing on the build plate, and the worst design when printing on a raft.

Automatic build orientation initialization (Crispo and Kim 2024a) was applied to the topology and build orientation optimization problem in Figure 25 with a critical search angle of $i_\theta = 5^\circ$ and with two angle step sizes for the coarse search of the orientation design space. The $\Delta = 45^\circ$ search converged to a poor local optimum in both cases, while the $\Delta = 15^\circ$ step size matched or beat the best results achieved in Figure 24. The coarser step size yielded a starting orientation of $\theta = (90^\circ, 90^\circ)$ for both the build plate and the raft, which converged to a poor local minimum angle in both cases. The fine step size instead selected an orientation of $\theta = (75^\circ, 0^\circ)$ and $\theta = (60^\circ, 0^\circ)$ for the build plate and raft runs, respectively. The $\Delta = 45^\circ$ search size had a negligible effect on the overall run time of the optimization, while the $\Delta = 15^\circ$ search resulted in a 5% increase in the total run time. The automatic approach achieved a strong topology and orientation solution, without needing to repeat the optimization with multiple initial orientation design variable vectors. However, the approach does not guarantee convergence to a strong local minimum, especially if a coarse step size is used.

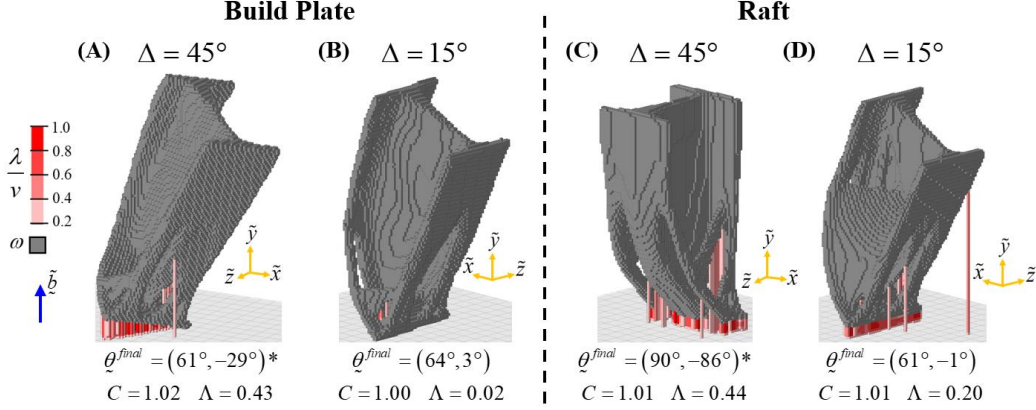


Figure 25 Simultaneous topology and build orientation optimization with automatic build orientation initialization using multiple angle search step sizes

Support structure volume and overhang area was plotted over the orientation design space for the baseline MBB result ($w=1$) with a 15% volume fraction over 3° steps in Figure 26. The final orientation of all topology and build orientation optimization results is also plotted, showing convergence to different local minima depending on the initialization. All automatic search results converged to the $45^\circ < \theta_1 < 135^\circ$ region. Comparing the overhang area and support structure volume design space, it is evident that support structure volume is more complex. Another important note is that there were regions with similar overhang area (such as $\theta_1 = -90^\circ$ and $\theta_1 = 90^\circ$) that had significantly different support structure volume. This is because the overhanging surfaces were at different distances from the build plate and therefore required different support structure volume.

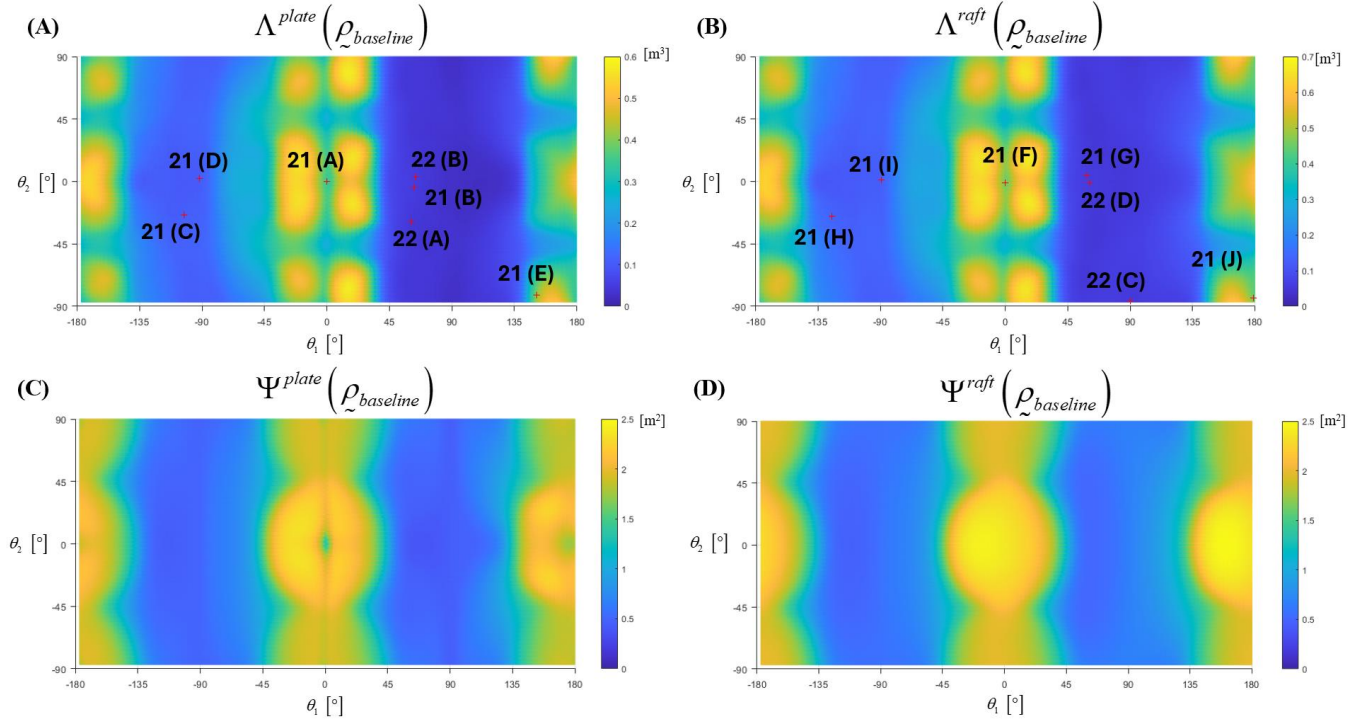


Figure 26 Plots of overhang area and support structure volume for the baseline TO result when printing on the build plate and on a raft, with the final orientation noted for each optimization result

Objective, constraint, and orientation design variable histories are plotted in Figure 27 for topology and build orientation optimization runs from Figure 24 (B) and Figure 25 (B), with a plot of AM density and support density included

for select iterations with a 0.1 iso threshold. In both cases, support structure volume (normalized relative to the volume of the component) was negative throughout the optimization as the designs evolved without support requirements. With automatic initialization in Figure 27 (B), support structure volume and orientation design variables were not active until iteration 5 as indicated by the dashed vertical line.

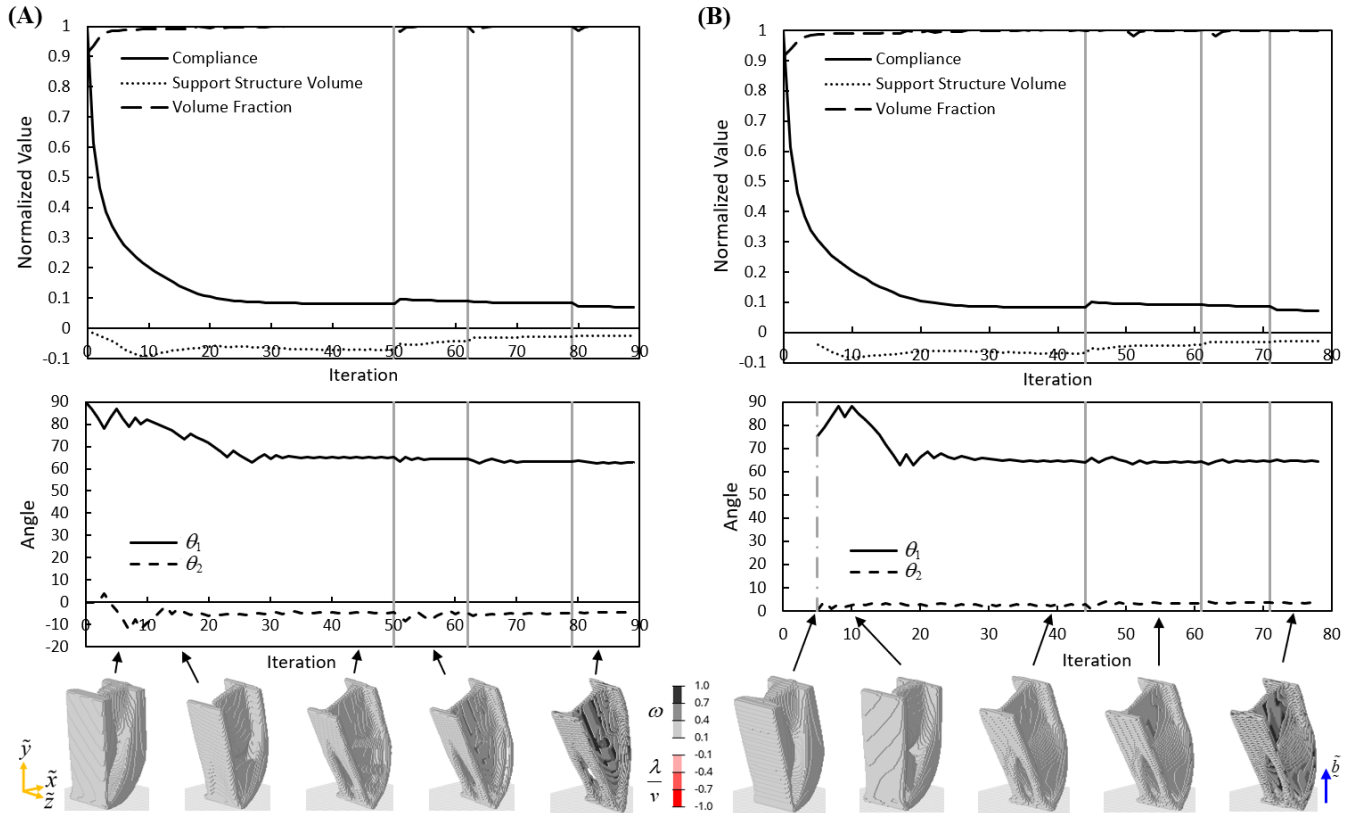


Figure 27 Convergence history for (A) standard orientation initialization, and (B) automatic orientation initialization

3.3. Multi-objective topology and build orientation optimization for support structure volume and overhang area

The difference between support structure volume and overhang area minimization in topology and build orientation optimization was investigated for the simply supported box and airplane bearing bracket problems from Figure 17 (C) and (D). The structural weighting factor was varied from $w=0.9$ to $w=0.3$ for three sets of AM cost weightings: only support structure volume ($q_\Lambda=1$, $q_\Psi=0$), only overhang area ($q_\Lambda=0$, $q_\Psi=1$), and both overhang area and support structure volume ($q_\Lambda=0.5$, $q_\Psi=0.5$). All results used the automatic build orientation initialization approach with a step size of $\Delta=15^\circ$, a volume fraction constraint of $\bar{V}=0.20$, and 5 layers of raft elements below the bottom of the part ($\eta_\mu^\lambda=-5$). Compliance was normalized relative to the lowest value across all results and AM objectives were normalized relative to the highest values.

A plot of support structure volume and overhang area for the simply supported box problem is shown in Figure 28. The AM and support density fields are shown in the print orientation and smoothed physical densities with a contour plot of overhang area are included in the boxed regions, showing a view of the bottom face. When considering only overhang area for $w=0.9$, the optimization converged to the orientation shown in Figure 28 (A1) with 44% lower overhang area relative to (A3) but required significant support structure volume. On the other hand, support structure minimization in Figure 28 (A3) converged to a result with 68% less support structure volume, but a larger overhanging surface. These two results demonstrate the difference between overhang area and support structure minimization,

because the distance of the overhanging surfaces from the build plate can significantly affect the support requirements. By considering both objectives, the result in Figure 28 (A2) converged to a similar orientation as (A3), but with small design modifications to reduce overhanging area by 24%. The $w=0.7$ results in Figure 28 (A4) – (A6) converged to similar orientations as their $w=0.9$ counterparts, but with design changes that further reduced overhang area and support structure volume. The (A5) result reduced both AM objectives significantly compared the (A1) and (A2) results with only a 1% increase in compliance. It should be noted that the $w=0.7$ structures have some small icicle features that become more significant at lower weighting factors (not pictured in Figure 28).

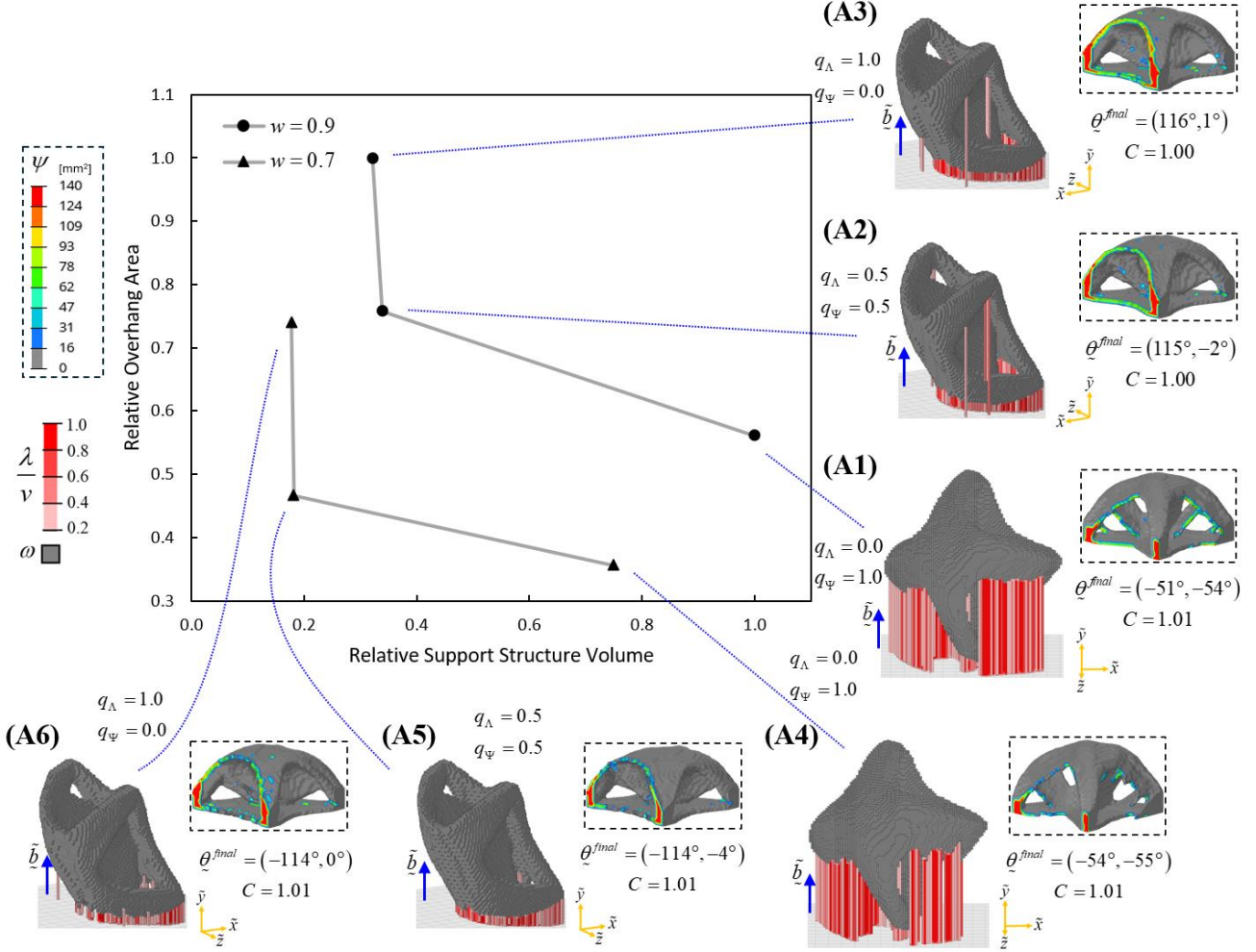


Figure 28 Plot of overhang area and support structure volume in topology and build orientation optimization for the simply supported box problem

Figure 29 shows a similar plot for the $w=0.7$ and $w=0.3$ results for the airplane bearing bracket problem, highlighting the trade-off between overhang area and support structure volume. The final orientations in Figure 29 (B1) and (B3) were 14° different, resulting in 62% and 45% reductions in overhang area or support structure, respectively, relative to each other. The design in Figure 29 (B6) rotated the component an additional 19° from (B3), such that the support columns initiating from the four mounting holes intersected the component. This change in orientation resulted in a large overhanging surface near the build plate but reduced the overall support structure volume, highlighting the difference between overhang and support structure objectives.

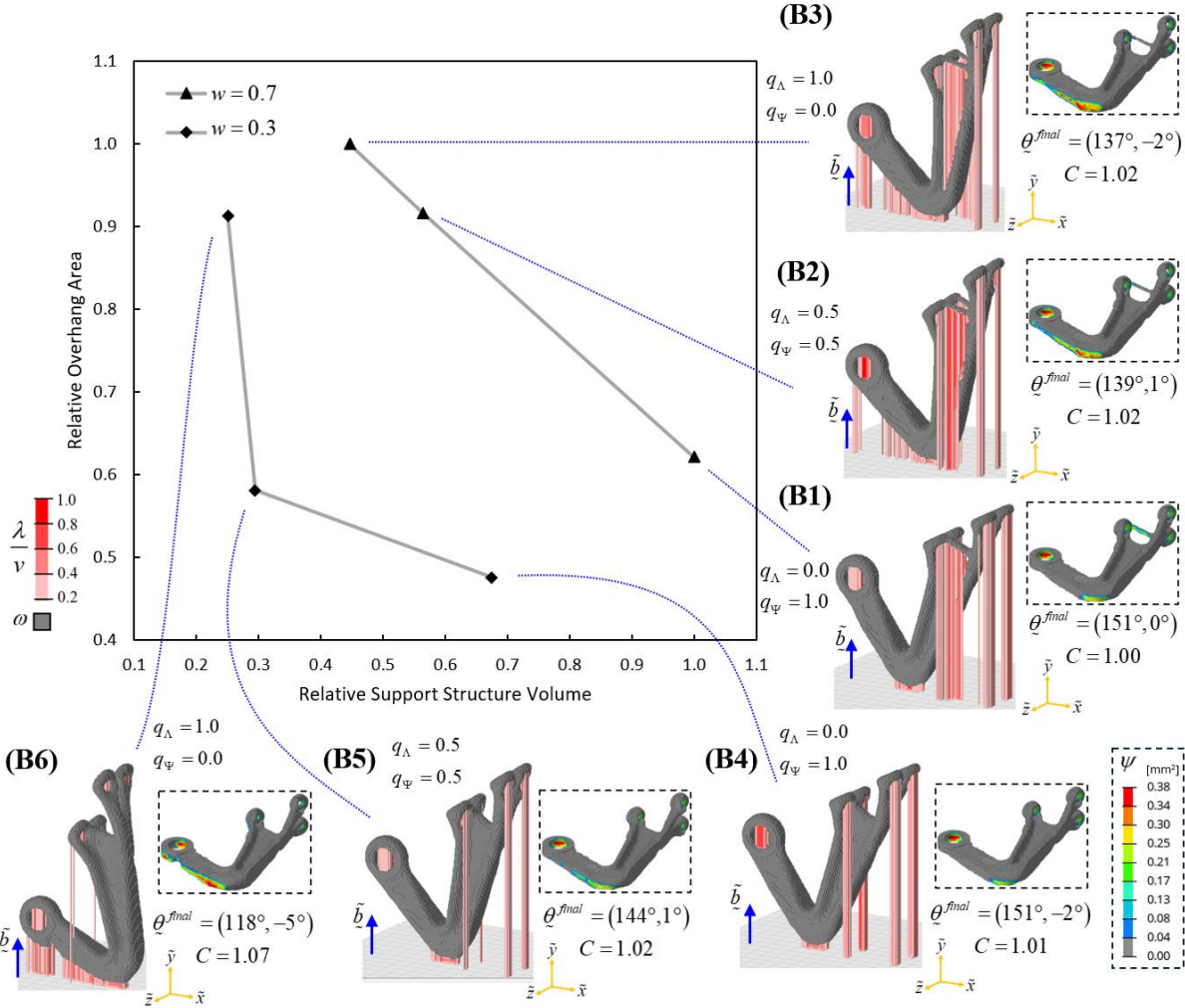


Figure 29 Plot of overhang area and support structure volume in topology and build orientation optimization for the airplane bearing bracket problem

It is clear from the results in Figure 28 and Figure 29 that a trade-off exists between support structure volume and overhang area objectives. In all cases, focusing on a single AM objective resulted in a significant increase in the other AM objective. Therefore, it is recommended to select weighting factor values such that both support structure and overhang area are considered during the optimization ($q_\Lambda \neq 0$ and $q_\Psi \neq 0$) to obtain a design that's favourable from both cost driving metrics. The exact weighting factor values should be assigned based on the relative importance of material use and post-processing cost driving factors for a given problem, as investigated further in Section 3.4.

3.4. Slicer validation

The support structure calculation used during optimization was specifically formulated for gradient-based topology and build orientation optimization and is therefore different from the support calculation used in slicer software. A slicer verification process was performed to validate that the results measured during optimization can be translated to reductions in realistic AM cost metrics. Results from Figure 28 and Figure 29 were post processed in Altair HyperView using an iso filter of smoothed physical density with an iso value of 0.3 to best capture all features of the optimized geometry. The geometry was smoothed using the ANSYS SpaceClaim “Shrinkwrap” and “smooth” functions. After smoothing, component volume had maximum variation of 1.6% and 3.4% for the box and airplane bracket, respectively. The results were sliced for FFF using PrusaSlicer v2.8.0 using the “Original Prusa XL – 2T Input Shaper 0.4 nozzle” preset

with “Generic PLA” filament, the “0.25mm STRUCTURAL” print settings, and automatic support generation. Select settings were modified as outlined in Table 2. The box problem was scaled to 10% of the original size for slicing (10cm \times 7.5cm \times 10cm). Relative Print Time and Relative Filament Used were directly output from the slicer software, and Relative Support Material Interface and Relative Support Material were obtained from the breakdown of material used for each feature. Filament use and print time correspond to the material use and print time cost driving factors, while support material and support material interface are estimations of the post processing time required to remove supports and improve surface finish.

Table 2 Slicer setting changes from “0.25mm STRUCTURAL” default values

Setting	Value
Generate Support Material	YES
Overhang Threshold	45°
Fill Density	30%
Perimeters	4
Raft Layers	3

Slicer validation for the box problem in Figure 28 is outlined in Table 3. In general, the overhang area and support structure volume reductions achieved during optimization translated to similar reductions in support material interface and support material slicer metrics. However, in some cases, such as in design (A6) the optimization estimated a 92% reduction in support structure, whereas the slicer calculated only a 59% reduction, both relative to design (A1). This occurred because the optimization uses simplified cost metrics, whereas the slicer software models the true printing process. In addition, the smoothing process introduces some geometry modifications from the original output TO densities. The differences between optimization and slicer calculations are highlighted in Figure 30 for design (A6). The boxed region in Figure 30 (A) and (B), zoomed in (D) and (E), shows a sharp corner in the AM mesh that met the self-supporting threshold and did not require support structure. This feature was smoothed during post-processing, resulting in the slicer identifying it as an overhang. Depending on the AM method, this overhanging region could be printed without supports with minor surface quality impacts, such as shown in Figure 30 (C) for FFF using the Prusa XL printer and the discussed slicer settings. While the support structures automatically generated by the slicer software could be manually adjusted for further support reduction, this was not done in this work to ensure a fair comparison between designs.

Table 3 Comparison of optimization objectives and slicer metrics for the simply supported box problem

Result	Relative Optimization Objectives						Relative Slicer Metrics			
	w	q_Λ	V	C	Ψ	Λ	Support Material Interface	Support Material	Print Time	Filament Used
(A1)	0.9	0	1.00	1.01	0.56	1.00	0.60	1.00	1.00	1.00
(A2)	0.9	0.5	1.00	1.00	0.76	0.34	0.81	0.44	0.92	0.93
(A3)	0.9	1	0.99	1.00	1.00	0.32	1.00	0.46	0.90	0.93
(A4)	0.7	0	1.01	1.01	0.36	0.75	0.46	0.85	1.05	1.01
(A5)	0.7	0.5	1.01	1.01	0.47	0.18	0.56	0.28	0.93	0.94
(A6)	0.7	1	0.99	1.01	0.74	0.18	0.87	0.41	0.89	0.92

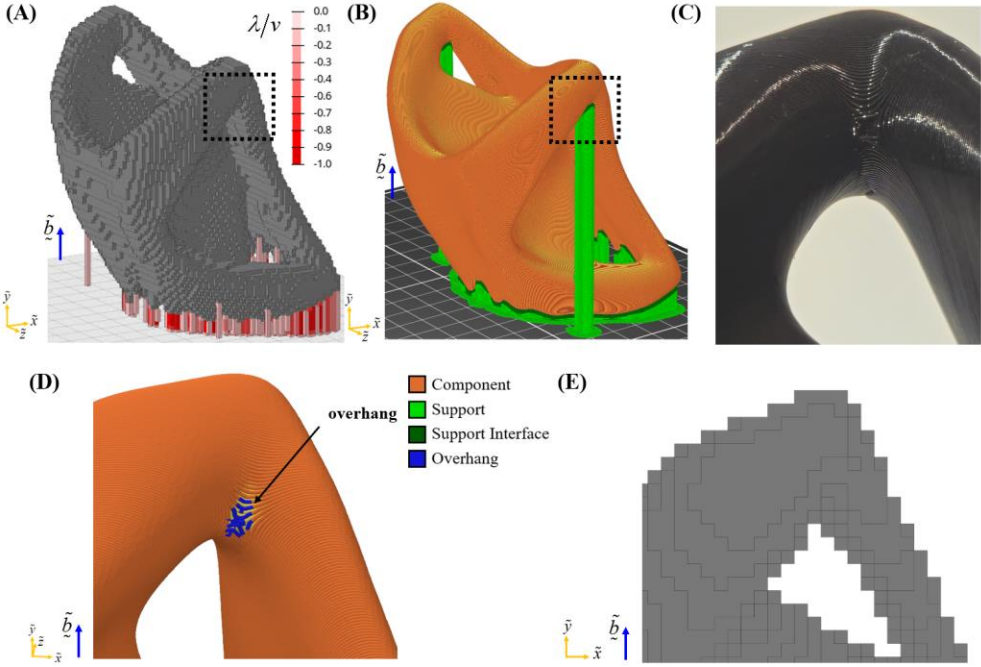


Figure 30 Comparison of support structure for design (A6): (A) optimization, (B) slicer software, (C) the boxed region printed using FFF without support structure, and (D)-(E) zoomed views of the boxed region

For the simply supported box problem, overhang area minimization in (A1) and (A4) resulted in the smallest support material interface, as expected, but yielded the longest print time and the most filament use. Support structure minimization in (A6) achieved an 11% reduction in print time and an 8% reduction filament use compared to the overhang result in (A1), but had a 45% increase in support material interface. Considering both overhang area and support structure volume in the optimization in (A2) and (A5) achieved similar print time and filament use to the support-only results in (A3) and (A6), with a 19% and 35% reduction in support material interface, respectively. Based on these results, it is recommended to include at least a small weighting on support structure volume in the optimization. This would help avoid convergence to orientations that minimize overhang but ultimately increase print time and filament use due to increased support structure requirements. Support structure optimization achieved the best design with (A6) showing the lowest printing time and filament use, however (A5) could be selected as an alternative with a reasonable trade-off between print time, material use, and post processing time.

It is also important to note that the slicer settings used for verification were selected to provide improved strength over the default settings by increasing the number of perimeters, which affect the strength and stiffness of the part (Schmitt et al. 2020). However, increasing the number of perimeters decreases the proportion of the overall time spent printing support material. For the result in (A1), perimeters contributed to 46% of the total printing time whereas infill and support material accounted for 21% and 13% of the print time, respectively. The default slicer settings with 15% infill and two perimeter layers would result in 18% of the print time allocated to support material, whereas a fully solid infill with four perimeters would result in 10% of the total print time spent on support material. It is therefore important to acknowledge that the savings in print time and material use depend on the exact slicer settings and the AM method used.

Slicer validation for the airplane bearing bracket is summarized in Table 4. For this problem, the reduction in overhang area calculated during optimization translated well to the support material interface slicer metric. However, for several designs, the reduction in support structure volume calculated during optimization did not correspond to a similar reduction in support material calculated during slicing. For example, design (B5) predicted a 71% reduction in support structure but only achieved a 29% support material reduction during slicing.

Table 4 Comparison of optimization objectives and slicer metrics for the airplane bearing bracket problem

Result	Relative Optimization Objectives						Relative Slicer Metrics			
	w	q_Λ	V	C	Ψ	Λ	Support Material Interface	Support Material	Print Time	Filament Used
(B1)	0.7	0	1.00	1.00	0.62	1.00	0.59	1.00	0.94	1.00
(B2)	0.7	0.5	0.99	1.02	0.92	0.56	0.98	1.08	1.02	1.02
(B3)	0.7	1	0.99	1.02	1.00	0.45	1.00	0.95	1.00	0.99
(B4)	0.3	0	1.00	1.01	0.48	0.67	0.47	0.75	0.91	0.95
(B5)	0.3	0.5	1.00	1.02	0.58	0.29	0.74	0.71	0.96	0.96
(B6)	0.3	1	0.97	1.07	0.91	0.25	0.80	0.48	0.91	0.89

The overhang area and support structure volume calculated during optimization are compared to the slicer output in Figure 31 for design (B5). In this case, the front surface had an angle of 44° , violating the self-supporting threshold by 1° . In the overhanging area calculation in Figure 31 (A), this surface was identified as a partial overhang because the smooth Heaviside calculation used in Eq. (13) outputs a value near 0.5 when the surface angle is very close to the self-supporting threshold. Figure 31 (B) shows that low density supports ($\lambda/v \approx 0.1$) were calculated for some portions of this surface, because of the smooth maximum function in Eq. (34) and possibly because the 1° violation in overhanging angle was not captured during the density mapping process. On the other hand, the slicer calculation in Figure 31 (C) identified this surface as violating the self-supporting threshold and added support material for the entire surface. Because this surface is very close to the self-supporting threshold angle, it could be printed using FFF as shown in Figure 31 (D) with the Prusa XL printer and the slicing settings outlined, but this may depend on the exact printing parameters.

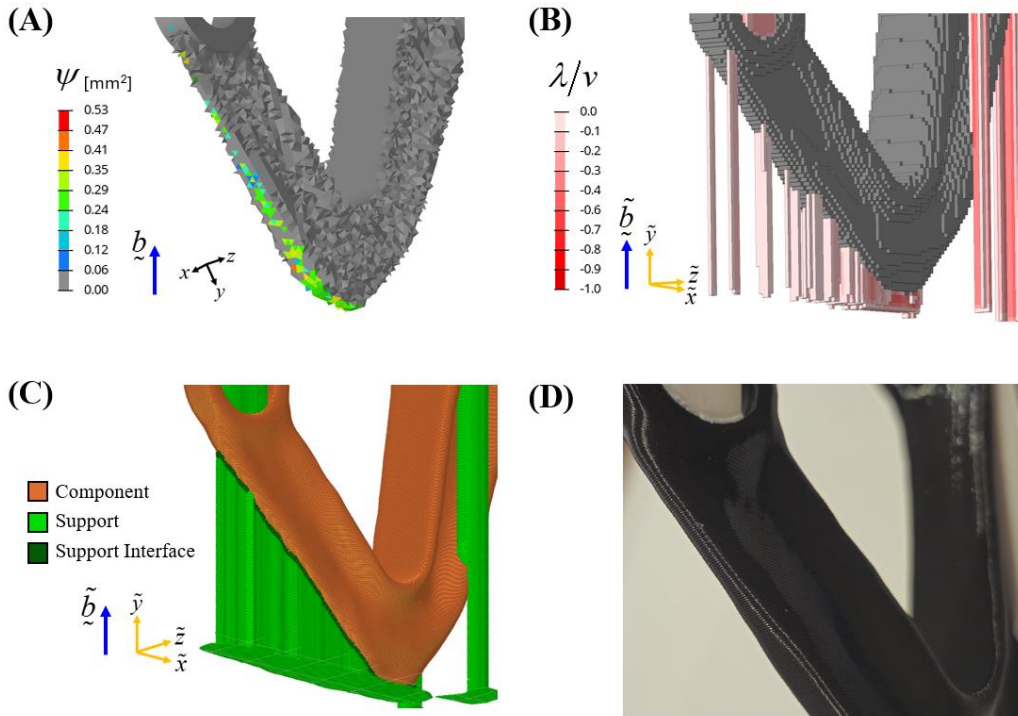


Figure 31 Comparison of the front surface of design (B5) showing (A) overhang, (B) support structure, (C) slicer calculations, and (D) the component printed with FFF without support structure for this surface

Further complicating the relationship between optimization and slicer metrics, the slicer software may place support material for surfaces that do not violate the self-supporting threshold (such as a surface angle of 46°), likely to ensure stability during printing. The discrepancies in support structure volume in (B2), (B3), and (B5) are due to the optimizer producing designs with surfaces at or within 1° of the self-supporting threshold that are classified as “partial overhangs” during optimization but required full support material during slicing. This could be avoided by slightly increasing the self-supporting threshold during optimization to account for how a given slicer addresses overhanging surfaces. In addition, the optimization smoothness parameters could be incrementally increased in subsequent phases to obtain a more accurate support structure and overhanging calculation in the final phases of the optimization. As with any design process, the results from the optimization and the support generated during slicing should be reviewed to ensure successful prints and to avoid unnecessary supports.

For the airplane bearing bracket problem with $w=0.7$, optimizations with only overhang or support structure minimization resulted in the same filament use, with design (B1) achieving a 6% lower printing time. With a larger weighting on AM cost, designs (B4) and (B6) achieved a 9% reduction in print time relative to design (B1), and design (B6) reduced filament use by 11% relative to design (B1). For both w weighting factors, the combined overhang and support optimization achieved worse results than either objective on their own, likely because of the slicer discrepancies discussed above. From the slicer results in Table 4, support structure minimization in design (B6) achieved the best results in terms of print time, filament use, and support material, but had a 7% increase in compliance relative to design (B1). If this increase in compliance was undesirable, design (B4) could be selected as an alternative design with equivalent print time, but higher material use relative to (B6). Results (B4) and (B6) from the proposed topology and build orientation optimization method are compared to a sequential TO and build orientation optimization in Figure 32. These designs were manufactured with PLA filament using the Original Prusa XL and the slicer settings outlined in Table 2, as shown in the second row images in Figure 32. Reductions in print time, filament use, and support interface were achieved by combined topology and build orientation optimization, with (B) showing a larger reduction in support interface, and (C) showing a larger reduction in support material.

(A) $\min : C(\underline{x}) \rightarrow \min : \Lambda(\theta)$ (B) $\min : C(\underline{x}) + \Psi(\underline{x}, \theta)$ (C) $\min : C(\underline{x}) + \Lambda(\underline{x}, \theta)$

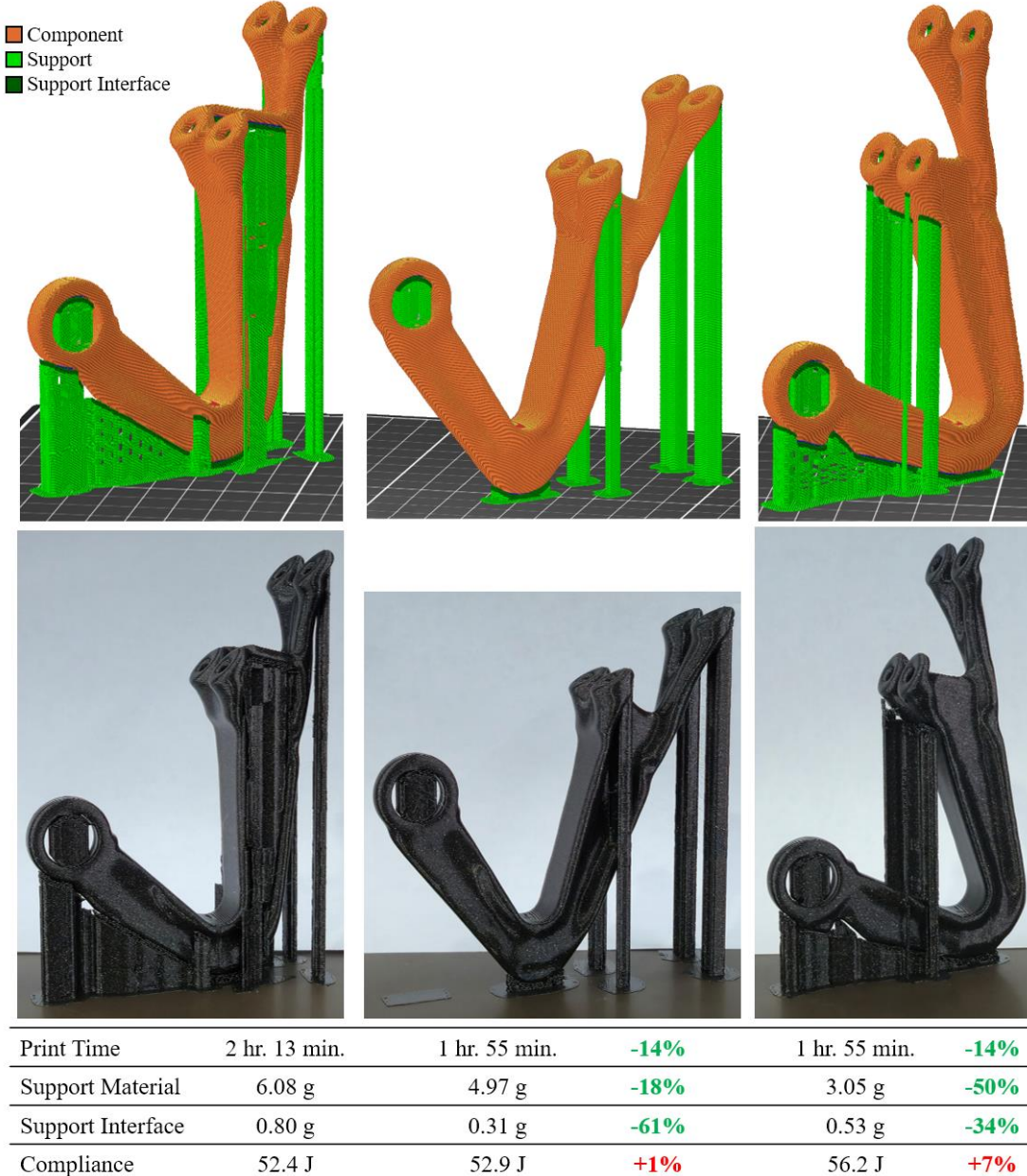


Figure 32 Comparison of slicer metrics and printed parts for optimization results from (A) traditional TO and BO methods applied sequentially, and topology and build orientation optimization for (B) overhang area, and (C) support structure volume

4. Conclusions

This paper presented an approach for support structure volume calculation in topology and build orientation optimization to minimize AM cost. A novel density mapping function was derived to map element densities from a rotated FE mesh to a structured AM mesh. This function is fully differentiable and can be applied to problems with 3D unstructured meshes. This mapping function allows for the calculation of response functions and their sensitivities with respect to the structured AM mesh densities, and sensitivities can be mapped back to the original element density and build orientation design variables. This work leveraged the mapping function to enable gradient-based topology

and build orientation optimization for support structure volume. A new support structure calculation was developed that allowed for direct minimization of support structure volume in the optimization problem statement, rather than relying on filtering or projection techniques that aim to produce self-supporting designs, which can be overly restrictive. The support structure calculation was also extended for any self-supporting threshold angle, allowing broad applicability of the approach with different AM processes.

The approach was verified using four numerical problems, including a realistic airplane bearing bracket test case. Fixed-orientation TO results showed the methodology was able to effectively minimize support structure volume with relatively small performance reductions, and in some cases generating self-supporting designs without any increase in compliance. The support structure volume objective had more local minima with respect to build orientation when compared to an overhang area objective due to the highly nonlinear nature of the function. However, the automatic build orientation initialization approach matched the best results from manual orientation initializations, albeit with a step size of 15° needed during the coarse orientation design space search.

Support structure minimization resulted in different final structures and orientations when compared with overhang area minimization. Overhang-focused topology and build orientation optimization converged to orientations with very low overhanging area, but the overhanging surfaces were often far from the build plate and required significant support structure volume. On the other hand, support structure minimization in topology and build orientation optimization converged to orientations with more overhanging surfaces that were lower to the build plate, ultimately reducing support structure volume. Slicer validation showed that support structure minimization achieved between 5% – 54% lower support material use and up to 15% lower print time relative to overhang area minimization. However, in some cases, the slicer validation resulted in significantly more support structure than calculated during optimization.

In future work, the linear support structure calculation used during optimization could be modified to more accurately represent a specific support type, such as the grid, snug, organic, or tree supports used in PrusaSlicer. Post-processing time could be more accurately modelled by calculating support structure attachment area (Langelaar 2016a) rather than overhanging area and by considering the ease of removal of support structure at the interior of the component (Sabiston and Kim 2020, Wang 2022, Wang et al. 2024). Build height and surface area objectives should also be incorporated into the AM cost model to achieve a holistic cost calculation. To further streamline the AM design workflow, an ideal topology and build orientation optimization method should also consider build volume constraints, physical performance and stability of support structures (Allaire and Bogosel 2018), thermal effects in metal parts, and anisotropic material properties.

Statements and Declarations

Funding information

This research was funded by the Natural Sciences and Engineering Research Council of Canada (NSERC).

Conflict of interest

The authors declare that they have no conflict of interest.

Author contributions

Conceptualization: Luke Crispo, Il Yong Kim; Methodology: Luke Crispo, Il Yong Kim; Formal analysis and investigation: Luke Crispo; Writing - original draft preparation: Luke Crispo; Writing - review and editing: Luke Crispo, Il Yong Kim; Supervision: Il Yong Kim; Software: Luke Crispo; Visualization: Luke Crispo.

Data availability

Not applicable.

Ethics approval

Not applicable.

Consent to participate

Not applicable.

Replication of results

The authors believe that sufficient information has been provided to reproduce the results presented in this paper. The methodology for density mapping and support structure calculation have been thoroughly described with references where appropriate. Sensitivity analysis for the developed methodology is included in Appendix A. Complete equations for smooth functions are included in Appendix B along with parameter values used in the optimization convergence scheme. A pseudo code is provided in Appendix C to show the overall workflow of the approach.

Appendix A. Sensitivity analysis for density mapping and support structure

Support structure sensitivity expressions are derived with respect to the filtered & thresholded AM densities $\partial\Lambda/\partial\omega_j$ and then adjusted to be in terms of the physical density and build orientation variables $\partial\Lambda/\partial\rho_i$ and $\partial\Lambda/\partial\theta_k$. The derivative of the total support structure volume with respect to a single j -th element is expressed in Eq. (A.1) as the sum of the partial derivative terms of that element's contribution to the support density of every element within the AM mesh.

$$\frac{\partial\Lambda}{\partial\omega_j} = \sum_{k \in N_{AM}} \frac{\partial\lambda_k}{\partial\omega_j} \quad (\text{A.1})$$

The derivative of the k -th element's support density with respect to the j -th element is defined as

$$\frac{\partial\lambda_k}{\partial\omega_j} = \frac{\partial\tau_k}{\partial\omega_j} v_k \mu_k^\lambda + \tau_k v_k \frac{\partial\mu_k^\lambda}{\partial\omega_j}. \quad (\text{A.2})$$

The derivative of the build plate indicator is calculated according to Eq. (A.3)-(A.4), where the j -th height indicator sensitivity term in Equation (A.5) depends only on its own density.

$$\frac{\partial\mu_k^\lambda}{\partial\omega_j} = -\frac{\partial S_H^{\mu^\lambda}(\tilde{r}_k^2 - B^\lambda)}{\partial(\tilde{r}_k^2 - B^\lambda)} \frac{\partial B^\lambda}{\partial\omega_j} \quad (\text{A.3})$$

$$\frac{\partial B^\lambda}{\partial\omega_j} = \frac{\partial S_{MIN}^\lambda(\hat{h}_j^\lambda)}{\partial\hat{h}_j^\lambda} \frac{\partial\hat{h}_j^\lambda}{\partial\omega_j} \quad (\text{A.4})$$

$$\frac{\partial\hat{h}_j^\lambda}{\partial\omega_j} = \tilde{r}_j^2 \frac{\partial S_H^{h^\lambda}(\omega_j)}{\partial\omega_j} \quad (\text{A.5})$$

The derivative of the generic smooth Heaviside and smooth maximum/minimum function are expressed in Eq. (A.6) and (A.7) for a generic a and c_i input, respectively.

$$\frac{\partial S_H^\square(a)}{\partial a} = \beta_\square \frac{1 - \tanh^2(\beta_\square(a - \eta_\square))}{\tanh(\beta_\square \eta_\square) + \tanh(\beta_\square(1 - \eta_\square))} \quad (\text{A.6})$$

$$\frac{\partial S_{MAX/MIN}^\square(c)}{\partial c_i} = \frac{\exp(\alpha_\square c_i)}{\sum_{i \in N} \exp(\alpha_\square c_i)} \left(1 + \alpha_\square (c_i - S_{MAX/MIN}^\square) \right) \quad (\text{A.7})$$

The derivative of the k -th element's support density with respect to the j -th element is defined in Eq. (A.8), with the support indicator derivatives expressed in Eq. (A.9) and (A.10). The Kronecker delta δ is equal to 1 if its two indexes are equal, and 0 otherwise. The i -th index in Eq. (A.9) refers to the element above the respective k -th element as depicted in Figure 10. The $\partial \tau_i / \partial \omega_j$ terms gets carried over from the i -th element above the k -th element as reducing the support volume in the i -th element will inherently reduce support volume in the k -th element. These terms get passed along the entire support column until the bottom of the AM mesh. The $\partial \zeta_i / \partial \omega_j$ term is non-zero only if $j \in N_i^S$ for the respective k -th element. Finally, the δ_{ij} term is active if the j -th element is immediately above the k -th element, and the δ_{kj} term is active if the j -th element is equal to the k -th element. As support density is set equal to zero for the top layer of elements ($\tau_k = 0$), the partial derivative term of support density for the top layer of elements is set to zero ($\partial \tau_k / \partial \omega_j = 0$).

$$\frac{\partial \tau_k}{\partial \omega_j} = \frac{\partial S_{MAX}^\tau(\bar{\tau}_k^1, \bar{\tau}_k^2, 0)}{\partial \bar{\tau}_k^1} \frac{\partial \bar{\tau}_k^1}{\partial \omega_j} + \frac{\partial S_{MAX}^\tau(\bar{\tau}_k^1, \bar{\tau}_k^2, 0)}{\partial \bar{\tau}_k^2} \frac{\partial \bar{\tau}_k^2}{\partial \omega_j}, \quad k \in N_j^C \quad (\text{A.8})$$

$$\frac{\partial \bar{\tau}_k^1}{\partial \omega_j} = \frac{\partial \tau_i}{\partial \omega_j} + \delta_{ij} - \frac{\partial \zeta_i}{\partial \omega_j}, \quad k \in N_j^C \quad (\text{A.9})$$

$$\frac{\partial \bar{\tau}_k^2}{\partial \omega_j} = \frac{\partial \tau_i}{\partial \omega_j} - \delta_{kj}, \quad k \in N_j^C \quad (\text{A.10})$$

Finally, the derivative of the i -th supporting indicator with respect to j -th AM density is calculated only for elements in which the j -th element belongs to the N_i^S supporting region as

$$\frac{\partial \zeta_i}{\partial \omega_j} = \begin{cases} \frac{\partial S_{MAX}^\zeta(\omega_k, \bar{\zeta}_i)}{\partial \omega_k} \delta_{kj} + \frac{\partial S_{MAX}^\zeta(\omega_k, \bar{\zeta}_i)}{\partial \bar{\zeta}_i^m} \frac{\partial \bar{\zeta}_i^m}{\partial \omega_j} & \bar{\alpha} \geq 60^\circ \\ \frac{\partial S_{MAX}^\zeta(\omega_j)_{j \in N_i^S}}{\partial \omega_j}, & \text{otherwise} \end{cases}, \quad (\text{A.11})$$

where δ_{kj} is the Kronecker delta and the intermediate supporting indicator sensitivity for $\bar{\alpha} \geq 60^\circ$ is calculated in Eq. (A.12) if the j -th element belongs to the $N_i^{S,m}$ supporting region.

$$\frac{\partial \bar{\zeta}_i^m}{\partial \omega_j} = \frac{\partial S_{MIN}^{\bar{\zeta}}(\omega_j)_{j \in N_i^{S,m}}}{\omega_j} \quad (\text{A.12})$$

The $\partial \tau_k / \partial \omega_j$ term in Eq. (A.8) is non-zero for only a select number of j -th elements in the AM mesh. A given j -th element's AM density influences the support density of the k -th elements through the supporting indicator only if it belongs to their associated N_i^S supporting regions through Eq. (31) and Figure 10. The j -th element's AM density also influences the support density of the element below it through Eq. (32) and its own support density through Eq. (33).

Finally, because each i -th support density influences the support density of the below k -th element in Eq. (34), the j -th element also affects the support density of all elements in vertical columns below these elements. This relationship is depicted in Figure A.1 for four sample elements in a simple 2D AM mesh, defining a new support column region N_j^C made up of these elements for which $\partial\tau_k/\partial\omega_j \neq 0$.

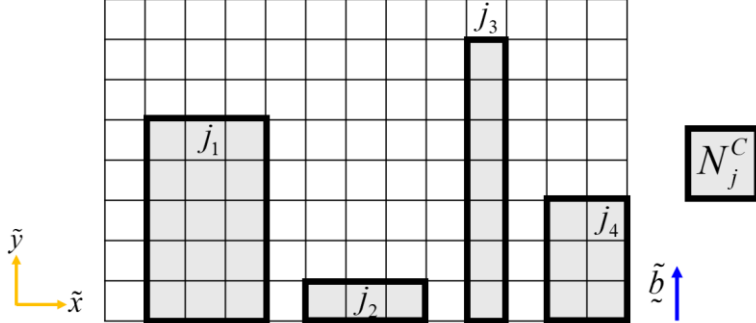


Figure A.1 Support column region for sensitivity analysis of four sample j -th elements

The majority of elements in the AM mesh will be similar to the j_1 element in Figure A.1, where the j -th AM density influences the support density of all i -th elements for which it is within the N_i^S supporting region, and all elements below. Elements at the top of the AM mesh, such as the j_3 element from Figure A.1, do not belong to any supporting regions and therefore only influence the support density of elements below itself. The j_2 and j_4 elements show examples of support column regions for elements that lie on the bottom and sides of the AM mesh, respectively.

When implementing these sensitivity calculations as expressed in Eq. (A.1)–(A.12), Eq. (A.11) is calculated immediately for all elements. Then, the support density derivatives $\partial\tau_k/\partial\omega_j$ of the top layer of elements are set to zero. Due to the layer-by-layer calculation of support density, Eq. (A.9), (A.10), and (A.8) should then be calculated one layer at a time, starting from the second highest layer of elements and moving downwards. Finally, the remaining expressions are calculated and Eq. (A.1) is used to calculate the total support structure sensitivities.

It should be noted that the above sensitivity formulation is computationally inefficient and not practical for large problems. The computational efficiency can be improved by substituting the support structure volume sensitivities from Eq. (A.2) into Eq. (A.1). In Eq. (A.13), the first summation is limited to the N_j^C support column region (where $\partial\tau_k/\partial\omega_j \neq 0$). The build plate indicator sensitivity from Eq. (A.3) is substituted into the second summation term and the constant $\partial B^\lambda/\partial\omega_j$ term is factored out of the summation. With this expression, the second summation does not depend on the j -th element and can therefore be calculated once per iteration for each k -th element and multiplied by the appropriate $\partial B^\lambda/\partial\omega_j$ term.

$$\begin{aligned} \frac{\partial\Lambda}{\partial\omega_j} &= \sum_{k \in N_{AM}} \left(\frac{\partial\tau_k}{\partial\omega_j} v_k \mu_k^\lambda + \tau_k v_k \frac{\partial\mu_k^\lambda}{\partial\omega_j} \right) \\ &= \sum_{k \in N_j^C} \frac{\partial\tau_k}{\partial\omega_j} v_k \mu_k^\lambda - \frac{\partial B^\lambda}{\partial\omega_j} \sum_{k \in N_{AM}} \tau_k v_k \frac{\partial S_H^{\mu^\lambda} (\tilde{r}_k^2 - B^\lambda)}{\partial(\tilde{r}_k^2 - B^\lambda)} \end{aligned} \quad (\text{A.13})$$

The $\partial\Lambda/\partial\omega_j$ sensitivities must then be adjusted for the filtering and thresholding steps to be in terms of the mapped AM densities as follows:

$$\frac{\partial\Lambda}{\partial\bar{\omega}_j} = \sum_{i \in N_j} \frac{\partial\Lambda}{\partial\omega_i} \frac{\partial\omega_i}{\partial\bar{\omega}_j}, \quad (\text{A.14})$$

$$\frac{\partial \omega_i}{\partial \bar{\omega}_j} = \frac{\partial S_H^o \left(\sum_{j \in N_i} \tilde{d}_{ji} \bar{\omega}_i / \sum_{j \in N_i} \tilde{d}_{ij} \right)}{\partial \left(\sum_{j \in N_i} \tilde{d}_{ji} \bar{\omega}_i / \sum_{j \in N_i} \tilde{d}_{ij} \right)} \frac{\tilde{d}_{ij}}{\sum_{j \in N_i} \tilde{d}_{ij}}. \quad (\text{A.15})$$

The derivative of support structure volume with respect to physical density and build orientation design variables is then calculated as

$$\frac{\partial \Lambda}{\partial \rho_e} = \sum_i \frac{\partial \Lambda}{\partial \bar{\omega}_i} \frac{\partial \bar{\omega}_i}{\partial \rho_e}, \quad (\text{A.16})$$

$$\frac{\partial \Lambda}{\partial \theta_k} = \sum_i \frac{\partial \Lambda}{\partial \bar{\omega}_i} \frac{\partial \bar{\omega}_i}{\partial \theta_k}, \quad (\text{A.17})$$

where the density mapping function sensitivity is expressed as follows:

$$\frac{\partial \bar{\omega}_i}{\partial \rho_e} = \frac{\gamma_{ie} v_e}{a_o}, \quad (\text{A.18})$$

$$\frac{\partial \bar{\omega}_i}{\partial \theta_k} = \frac{1}{a_o} \sum_e \frac{\partial \gamma_{ie}}{\partial \theta_k} v_e \rho_e. \quad (\text{A.19})$$

The γ_{ie} weighting term is a function of build orientation design variables, and its derivative is calculated as

$$\frac{\partial \gamma_{ie}}{\partial \theta_k} = \frac{\partial S_R^\gamma \left(\|\tilde{s}_{ie}\| \right)}{\partial \|\tilde{s}_{ie}\|} \frac{\partial \|\tilde{s}_{ie}\|}{\partial \theta_k}, \quad (\text{A.20})$$

where the reverse smooth Heaviside sensitivity is expressed as

$$\frac{\partial S_R^\square(a)}{\partial a} = \begin{cases} 0, & a > 2\eta_\square \\ \frac{3}{\eta_\square} \left(\left(\frac{a}{2\eta_\square} \right)^2 - \frac{a}{2\eta_\square} \right), & \text{otherwise} \end{cases}. \quad (\text{A.21})$$

The derivative of the magnitude of the vector between FE and AM elements is calculated as

$$\frac{\partial \|\tilde{s}_{ie}\|}{\partial \theta_k} = \frac{\tilde{s}_{ie}}{\|\tilde{s}_{ie}\|} \cdot \frac{\partial \tilde{s}_{ie}}{\partial \theta_k}, \quad (\text{A.22})$$

$$\frac{\partial \tilde{s}_{ie}}{\partial \theta_k} = - \frac{\partial \tilde{r}_e}{\partial \theta_k}, \quad (\text{A.23})$$

$$\frac{\partial \tilde{r}_e}{\partial \theta_k} = \frac{\partial R^T}{\partial \theta_k} \tilde{r}_e, \quad (\text{A.24})$$

where the transpose of the partial derivatives of the rotation matrix in Eq. (A.25)-(A.26).

$$\frac{\partial R}{\partial \theta_1} = \begin{bmatrix} -\sin \theta_1 & -\cos \theta_1 & 0 \\ \cos \theta_2 \cos \theta_1 & -\cos \theta_2 \sin \theta_1 & 0 \\ \sin \theta_2 \cos \theta_1 & -\sin \theta_2 \sin \theta_1 & 0 \end{bmatrix} \quad (\text{A.25})$$

$$\frac{\partial \tilde{R}}{\partial \theta_2} = \begin{bmatrix} 0 & 0 & 0 \\ -\sin \theta_2 \sin \theta_1 & -\sin \theta_2 \cos \theta_1 & -\cos \theta_2 \\ \cos \theta_2 \sin \theta_1 & \cos \theta_2 \cos \theta_1 & -\sin \theta_2 \end{bmatrix} \quad (\text{A.26})$$

Finally, all sensitivities derived with respect to physical densities are adjusted to be expressed in terms of the element density design variables. This process is illustrated for a generic response as

$$\frac{\partial \square}{\partial \tilde{x}_i} = \sum_{e \in N_i} \frac{\partial \square}{\partial \rho_e} \frac{\partial \rho_e}{\partial \tilde{x}_i} \frac{\partial \tilde{x}_e}{\partial x_i}, \quad (\text{A.27})$$

where sensitivities are summed for all neighbouring elements belonging to N_i and are multiplied by the sensitivity terms of the filtered and thresholded density as follows:

$$\frac{\partial \tilde{x}_e}{\partial x_i} = \frac{d_{ei} v_i}{\sum_{i \in N_e} d_{ei} v_i}, \quad (\text{A.28})$$

$$\frac{\partial \rho_e}{\partial \tilde{x}_e} = \frac{\partial S_H^\rho(\tilde{x}_e)}{\partial \tilde{x}_e}. \quad (\text{A.29})$$

Support structure and density mapping sensitivities are verified using the finite difference method for a sample 2D cantilever beam problem with 4000 elements at iteration 5 with a build orientation of $\theta_1 = -5^\circ$, shown in Figure A.2 (A). Analytical sensitivities are plotted in Figure A.2 (B) and finite difference sensitivities are plotted in Figure A.2 (C) using a step size of $\Delta \rho = 10^{-6}$. Excellent agreement is shown qualitatively in Figure A.2 (D), with 99% of sensitivities within 0.01% agreement. The agreement term was not calculated for gray elements that have near-zero sensitivities to avoid roundoff errors. Table A.1 provides numerical sensitivity verification for the randomly selected boxed elements in Figure A.2 (A), showing nearly perfect agreement. Build orientation sensitivity with a step size of $\Delta \theta = 0.0001$ radians had strong agreement with $(\Delta \Lambda / \Delta \theta_1) / (\partial \Lambda / \partial \theta_1) = 100.090\%$.

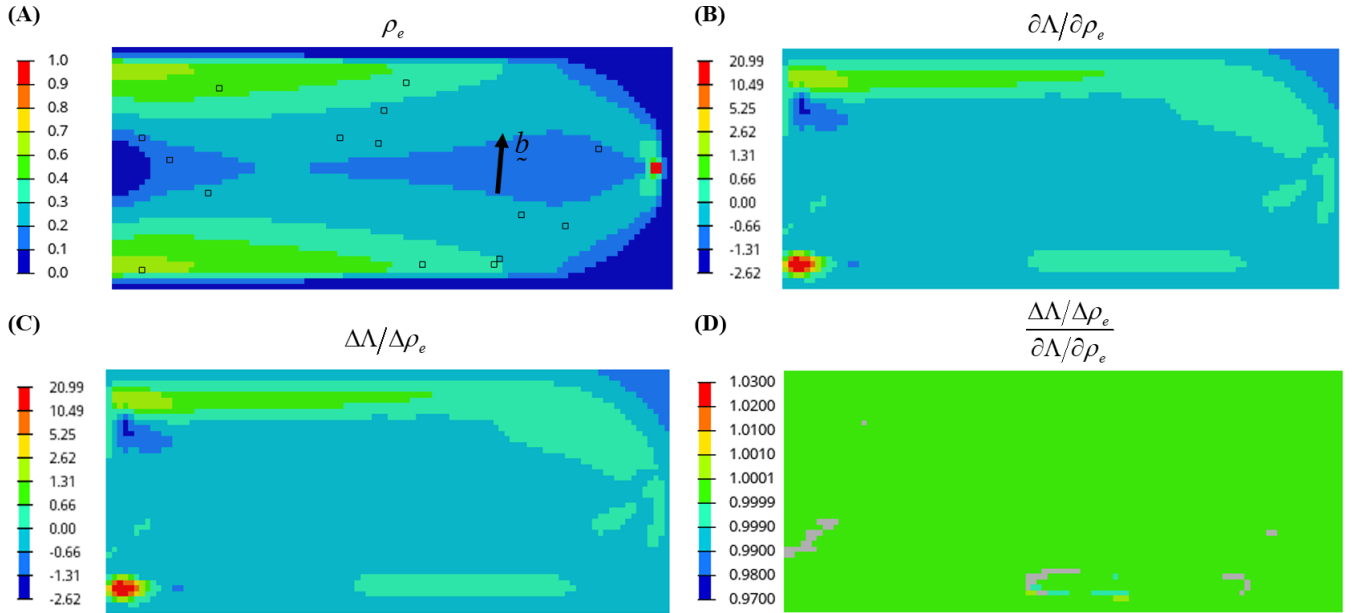


Figure A.2 Complete sensitivity verification of support structure volume with respect to element physical density

Table A.1 Select sensitivity verification of support structure volume with respect to element physical density

Element <i>e</i>	Finite Difference Sensitivity $\Delta\Lambda/\Delta\rho_e \times 10^3$	Analytical Sensitivity $\partial\Lambda/\partial\rho_e \times 10^3$	Agreement $\frac{\Delta\Lambda/\Delta\rho_e}{\partial\Lambda/\partial\rho_e} \times 100\%$
2992	-0.17664	-0.17664	100.000%
3839	3.43473	3.43472	100.000%
929	-0.05052	-0.05052	100.000%
1259	-0.00306	-0.00306	100.000%
1370	0.00184	0.00184	100.000%
2887	-0.10307	-0.10307	100.000%
3466	-0.15117	-0.15117	100.000%
2758	-0.23781	-0.23781	100.000%
1378	0.00268	0.00268	100.000%
3502	0.65414	0.65414	100.000%
1613	0.48878	0.48878	100.000%
3991	-0.35351	-0.35351	100.000%
1125	0.00193	0.00193	100.000%
156	-0.00140	-0.00140	100.000%
3235	-0.00258	-0.00258	100.000%

Appendix B. Smooth functions and parameter values

Table B.1 Complete equations for smooth functions and the associated parameter values

Equation Number	Expanded Equation	Parameter Values
(4)	$\rho_e(\tilde{x}) = S_H^\rho(\bar{x}_e) = \frac{\tanh(\beta_\rho \eta_\rho) + \tanh(\beta_\rho (\bar{x}_e - \eta_\rho))}{\tanh(\beta_\rho \eta_\rho) + \tanh(\beta_\rho (1 - \eta_\rho))}$	$\beta_\rho = [1, 2, 4, 8]$ $\eta_\rho = 0.5$
(11)	$\begin{aligned} \phi_e(\tilde{x}) &= \frac{v_e^{2/3}}{a_\phi} S_H^\phi(\ \nabla \rho_e\) \\ &= \frac{v_e^{2/3}}{a_\phi} \frac{\tanh(\beta_\phi \eta_\phi) + \tanh(\beta_\phi (\ \nabla \rho_e\ - \eta_\phi))}{2 \tanh(\beta_\phi \eta_\phi)} \end{aligned}$	$\beta_\phi = 8$ $\eta_\phi = 0.08$
(13)	$\begin{aligned} \psi_e^{\text{raft}}(\tilde{x}, \theta) &= \phi_e S_H^\psi(\cos \alpha_e) \\ &= \phi_e \frac{\tanh(\beta_\psi (1 + \eta_\psi)) + \tanh(\beta_\psi (\cos \alpha_e - \eta_\psi))}{\tanh(\beta_\psi (1 + \eta_\psi)) + \tanh(\beta_\psi (1 - \eta_\psi))} \end{aligned}$	$\beta_\psi = 10$ $\eta_\phi = \cos \bar{\alpha}$
(16)	$\begin{aligned} \hat{h}_e^\psi(\tilde{x}, \theta) &= (h_e - \bar{h}) S_H^{h^\psi}(\rho_e) \\ &= (h_e - \bar{h}) \frac{\tanh(\beta_h^\psi \eta_h^\psi) + \tanh(\beta_h^\psi (\rho_e - \eta_h^\psi))}{\tanh(\beta_h^\psi \eta_h^\psi) + \tanh(\beta_h^\psi (1 - \eta_h^\psi))} \\ &= (h_e - \bar{h}) \frac{\tanh(\beta_h^\psi \rho_e)}{\tanh(\beta_h^\psi)}, \quad \eta_h^\psi = 0 \end{aligned}$	$\beta_h^\psi = [1, 2, 4, 8]$ $\eta_h^\psi = 0$
(17)	$B^\psi(\tilde{x}, \theta) = S_{MN}^\psi(\hat{h}^\psi) = \frac{\sum_i \hat{h}_i^\psi \exp(\alpha_B^\psi \hat{h}_i^\psi)}{\sum_i \exp(\alpha_B^\psi \hat{h}_i^\psi)}, \quad i \in N_p$	$\alpha_B^\psi = -50$
(19)	$\begin{aligned} \mu_e(\tilde{x}, \theta) &= S_H^\mu(h_e - \bar{h} - B^\psi) \\ &= \frac{\tanh(\beta_\mu (1 + \eta_\mu)) + \tanh(\beta_\mu (h_e - \bar{h} - B^\psi - \eta_\mu))}{\tanh(\beta_\mu (1 + \eta_\mu)) + \tanh(\beta_\mu (1 - \eta_\mu))} \end{aligned}$	$\beta_\mu = [12, 24, 48, 96]$ $\eta_\mu = [4, 2, 0, -2]$
(26)	$\gamma_{ie}(\theta) = S_R^\gamma(\ \tilde{s}_{ie}\) = \begin{cases} 0, & \ \tilde{s}_{ie}\ > 2\eta_\gamma \\ 2\left(\frac{\ \tilde{s}_{ie}\ }{2\eta_\gamma}\right)^3 - 3\left(\frac{\ \tilde{s}_{ie}\ }{2\eta_\gamma}\right)^2 + 1, & \text{otherwise} \end{cases}$	$\eta_\gamma = [1.25, 1.0, 1.0, 1.0]$
(30)	$\begin{aligned} \omega_i(\tilde{x}, \theta) &= S_H^\omega\left(\frac{\sum_j d_{ij} \bar{\omega}_j}{\sum_j d_{ij}}\right), \quad j \in N_i \\ &= \frac{\tanh(\beta_\omega \eta_\omega) + \tanh\left(\beta_\omega \left(\frac{\sum_j d_{ij} \bar{\omega}_j}{\sum_j d_{ij}} - \eta_\omega\right)\right)}{\tanh(\beta_\omega \eta_\omega) + \tanh(\beta_\omega (1 - \eta_\omega))}, \quad j \in N_i \end{aligned}$	$\beta_\omega = [1, 2, 4, 8]$ $\eta_\omega = [0.5, 0.45, 0.4, 0.35]$

Equation Number	Expanded Equation	Parameter Values
(31) / (40)	$\zeta_i(x, \theta) = \begin{cases} S_{MAX}^{\zeta}(\omega_k, \bar{\zeta}_i), & \bar{\alpha} \geq 60^\circ \\ S_{MAX}^{\zeta}(\omega_j)_{j \in N_i^S}, & \text{otherwise} \end{cases}$ $= \begin{cases} \frac{\omega_k \exp(\alpha_\zeta \omega_k) + \sum_{m=1,4} \bar{\zeta}_i^m \exp(\alpha_\zeta \bar{\zeta}_i^m)}{e^{\alpha_\zeta \omega_k} + \sum_{m=1,4} \exp(\alpha_\zeta \bar{\zeta}_i^m)}, & \bar{\alpha} \geq 60^\circ \\ \frac{\sum_{j \in N_i^S} \omega_j \exp(\alpha_\zeta \omega_j)}{\sum_{j \in N_i^S} \exp(\alpha_\zeta \omega_j)}, & \text{otherwise} \end{cases}$	$\alpha_\zeta = 15$
(34)	$\tau_k(x, \theta) = S_{MAX}^\tau(\bar{\tau}_k^1, \bar{\tau}_k^2, 0) = \frac{\bar{\tau}_k^1 \exp(\alpha_\tau \bar{\tau}_k^1) + \bar{\tau}_k^2 \exp(\alpha_\tau \bar{\tau}_k^2)}{\exp(\alpha_\tau \bar{\tau}_k^1) + \exp(\alpha_\tau \bar{\tau}_k^2) + 1}$	$\alpha_\tau = 15$
(35)	$\hat{h}_k^\lambda(x, \theta) = \tilde{r}_k^2 S_H^{h^\lambda}(\omega_k) = \tilde{r}_k^2 \frac{\tanh(\beta_h^\lambda \eta_h^\lambda) + \tanh(\beta_h^\lambda (\omega_k - \eta_h^\lambda))}{\tanh(\beta_h^\lambda \eta_h^\lambda) + \tanh(\beta_h^\lambda (1 - \eta_h^\lambda))}$ $= \tilde{r}_k^2 \frac{\tanh(\beta_h^\lambda \omega_k)}{\tanh(\beta_h^\lambda)}, \quad \eta_h = 0$	$\beta_h^\lambda = [1, 2, 4, 8]$ $\eta_h^\lambda = 0$
(36)	$B^\lambda(x, \theta) = S_{MIN}^\lambda(\hat{h}^\lambda) = \frac{\sum_k \hat{h}_k^\lambda \exp(\alpha_B^\lambda \hat{h}_k^\lambda)}{\sum_k \exp(\alpha_B^\lambda \hat{h}_k^\lambda)}, \quad k \in N_{AM}$	$\alpha_B^\lambda = -50$
(37)	$\mu_k^\lambda(x, \theta) = S_H^{\mu^\lambda}(\tilde{r}_k^2 - B^\lambda)$ $= \frac{\tanh(\beta_\mu^\lambda (1 + \eta_\mu^\lambda)) + \tanh(\beta_\mu^\lambda (\tilde{r}_k^2 - B^\lambda - \eta_\mu^\lambda))}{\tanh(\beta_\mu^\lambda (1 + \eta_\mu^\lambda)) + \tanh(\beta_\mu^\lambda (1 - \eta_\mu^\lambda))}$	$\beta_\mu^\lambda = [8, 16, 32, 64]$ plate : $\eta_\mu^\lambda = 0$ raft : $\eta_\mu^\lambda = -\# \text{ raft layers}$
(42)	$\bar{\zeta}_i^m(x, \theta) = S_{MIN}^{\bar{\zeta}}(\omega_j)_{j \in N_i^{S,m}} = \frac{\sum_{j \in N_i^{S,m}} \omega_j \exp(\alpha_{\bar{\zeta}} \omega_j)}{\sum_{j \in N_i^{S,m}} \exp(\alpha_{\bar{\zeta}} \omega_j)}$	$\alpha_{\bar{\zeta}} = -15$

Appendix C. Pseudo code

```

! Overview of density mapping and support structure volume calculation
SUBROUTINE SUPPORT_CALCULATION(DENS, BUILD_OR, CENTERS, SUP_VOL, SENS)
    ! Define input/output variables
    REAL, INTENT(IN) :: DENS(NUM_ELEMS) ! element physical densities
    REAL, INTENT(IN) :: BUILD_OR(3) ! build orientation vector
    REAL, INTENT(IN) :: CENTERS(NUM_ELEMS,3) ! element centroid locations
    REAL, INTENT(OUT) :: SUP_VOL ! total support structure volume
    REAL, INTENT(OUT) :: SENS(NUM_ELEMS+2) ! physical density and orientation derivatives

    ! Initialize structured AM mesh and calculate AM mesh element centroids
    AM_CENTERS = INITIALIZE_AM_MESH(CENTERS)

    ! Rotate FE mesh based on build orientation
    ROT_CENTERS = ROTATE_FE_MESH(CENTERS, BUILD_OR)

    ! Map FE physical densities to structured AM densities based on centroid distances
    AM_DENS = MAP_FE_AM_DENSITIES(DENS, ROT_CENTERS, AM_CENTERS)

    ! Threshold and filter AM densities
    CALL FILTER_THRES_DENSITIES(AM_DENS)

    ! Calculate build plate indicator for all AM elements
    BP_INDC = CALC_BUILD_PLATE_INDC(AM_DENS, AM_CENTERS)

    ! Calculate supporting indicator for all AM elements
    SUP_INDC = CALC_SUPPORTING_INDC(AM_DENS)

    ! Calculate support structure volume one layer at a time
    DO LAYER = NUM_LAYERS, 1, -1
        IF (LAYER == NUM_LAYERS) THEN
            ! Set support structure density for the top layer equal to zero
            SUP_DENS_LAYER = 0
        ELSE
            ! Calculate temporary support indicator 1 and 2 for current layer
            SI_TEMP1 = CALC_SUPPORT_INDC_1(SUP_DENS_LAYER, AM_DENS, SUP_INDC, LAYER)
            SI_TEMP2 = CALC_SUPPORT_INDC_2(SUP_DENS_LAYER, AM_DENS, LAYER)
            ! Calculate support structure density for current layer
            SUP_DENS_LAYER = CALC_SUPPORT_DENSITY_LAYER(SI_TEMP1, SI_TEMP2)
        END IF
        ! Insert support density values for current layer into overall support density variable
        CALL INSERT_SUPPORT_DENSITY(SUP_DENS, SUP_DENS_LAYER)
    END DO

    ! Calculate total support structure volume
    SUP_VOL = SUM(SUP_DENS * BP_INDC) * AM_MESH_VOL

    ! Calculate total support structure volume sensitivities for AM densities (full detail omitted)
    SENS_AM = CALC_SUPPORT_VOLUME_SENSITIVITIES(DENS, BUILD_OR, CENTERS)

    ! Adjust sensitivities for filtering and thresholding steps
    CALL FILTER_THRES_SENS(SENS_AM)

    ! Convert from AM sensitivities to physical density and orientation sensitivities
    SENS = MAP_AM_FE_SENS(SENS_AM, DENS, ROT_CENTERS, AM_CENTERS)

END SUBROUTINE SUPPORT_CALCULATION

```

References

- Allaire, G, Bogosel, B (2018) Optimizing supports for additive manufacturing. 58(6):2493-2515. <https://doi.org/10.1007/s00158-018-2125-x>
- Allaire, G, Dapogny, C, Estevez, R, Faure, A, Michailidis, G (2017) Structural optimization under overhang constraints imposed by additive manufacturing technologies. J Comput Phys 351:295-328. <https://doi.org/10.1016/j.jcp.2017.09.041>
- Bendsoe, MP, Sigmund, O (1999) Material interpolation schemes in topology optimization. Arch. Appl. Mech. 69(9-10):635-654. <https://doi.org/10.1007/s004190050248>
- Brika, SE, Zhao, YF, Brochu, M, Mezzetta, J (2017) Multi-Objective Build Orientation Optimization for Powder Bed Fusion by Laser. 139(11):1-8. <https://doi.org/10.1115/1.4037570>
- Chen, H, Joglekar, A, Whitefoot, KS, Burak Kara, L (2023) Concurrent Build Direction, Part Segmentation, and Topology Optimization for Additive Manufacturing Using Neural Networks. J Mech Des 145(9):1-14. <https://doi.org/10.1115/1.4062663>
- Cheng, L, To, A (2019) Part-scale build orientation optimization for minimizing residual stress and support volume for metal additive manufacturing: Theory and experimental validation. Comput Aided Des 113:1-23. <https://doi.org/10.1016/j.cad.2019.03.004>
- Clausen, A, Andreassen, E (2017) On filter boundary conditions in topology optimization. Struct Multidiscip Optim 56(5):1147-1155. <https://doi.org/10.1007/s00158-017-1709-1>
- Crispo, L, Kim, IY (2024a) Topology and build orientation optimization for additive manufacturing considering build height and overhang area. 67(6):1-36. <https://doi.org/10.1007/s00158-024-03808-9>
- Crispo, L, Kim, IY (2024b) Topology and Build Orientation Optimization for Additive Manufacturing: Influence of Printing on Raft and Build Plate. In: Proceedings of the WCX SAE World Congress Experience, Detroit, USA, pp. 1-10
- Daynes, S (2022) Simultaneous optimisation of support structure regions and part topology for additive manufacturing. 65(11):334. <https://doi.org/10.1007/s00158-022-03454-z>
- Fritz, K, Kim, IY (2020) Simultaneous topology and build orientation optimization for minimization of additive manufacturing cost and time. Int J Numer Methods Eng 121(15):3442-3481. <https://doi.org/10.1002/nme.6366>
- Garaigordobil, A, Ansola, R, de Bustos, IF (2021) On preventing the dripping effect of overhang constraints in topology optimization for additive manufacturing. Struct Multidiscip Optim 64(6):4065-4078. <https://doi.org/10.1007/s00158-021-03077-w>
- Garaigordobil, A, Ansola, R, Santamaria, J, de Bustos, IF (2018) A new overhang constraint for topology optimization of self-supporting structures in additive manufacturing. Struct Multidiscip Optim 58(5):2003-2017. <https://doi.org/10.1007/s00158-018-2010-7>
- Gaynor, AT, Guest, JK (2016) Topology optimization considering overhang constraints: Eliminating sacrificial support material in additive manufacturing through design. Struct Multidiscip Optim 54(5):1157-1172. <https://doi.org/10.1007/s00158-016-1551-x>
- GrabCAD. (2016). "Airplane Bearing Bracket Challenge." Retrieved July 29, 2024, from <https://grabcad.com/challenges/airplane-bearing-bracket-challenge>.
- Huang, RZ, Riddle, M, Graziano, D, Warren, J, Das, S, Nimbalkar, S, Cresko, J, Masanet, E (2016) Energy and emissions saving potential of additive manufacturing: the case of lightweight aircraft components. J Clean Prod 135:1559-1570. <https://doi.org/10.1016/j.jclepro.2015.04.109>
- Ibhadode, O, Zhang, Z, Sixt, J, Nsiempba, KM, Orakwe, J, Martinez-Marchese, A, Ero, O, Shahabad, SI, Bonakdar, A, Toyserkani, E (2023) Topology optimization for metal additive manufacturing: current trends, challenges, and future outlook. 18(1):e2181192. <https://doi.org/10.1080/17452759.2023.2181192>
- Inc., AE (2023) Altair OptiStruct Reference Guide 2023.1, Altair Engineering Inc.
- Jiang, J, Stringer, J, Xu, X, Zhong, RY (2018a) Investigation of printable threshold overhang angle in extrusion-based additive manufacturing for reducing support waste. 31(10):961-969. <https://doi.org/10.1080/0951192X.2018.1466398>
- Jiang, JC, Xu, X, Stringer, J (2018b) Support Structures for Additive Manufacturing: A Review. J. Manuf. Mater. Process. 2(4):1-23. <https://doi.org/10.3390/jmmp2040064>

- Langelaar, M (2016a) Topology optimization for additive manufacturing with controllable support structure costs. In: Proceedings of the Proceedings of the 7th European Congress on Computational Methods in Applied Sciences and Engineering, Crete, Greece, pp. 3689-3699
- Langelaar, M (2016b) Topology optimization of 3D self-supporting structures for additive manufacturing. *Addit Manuf* 12:60-70. <https://doi.org/10.1016/j.addma.2016.06.010>
- Langelaar, M (2017) An additive manufacturing filter for topology optimization of print-ready designs. *Struct Multidiscip Optim* 55(3):871-883. <https://doi.org/10.1007/s00158-016-1522-2>
- Langelaar, M (2018) Combined optimization of part topology, support structure layout and build orientation for additive manufacturing. *Struct Multidiscip Optim* 57(5):1985-2004. <https://doi.org/10.1007/s00158-017-1877-z>
- Lazarov, BS, Sigmund, O (2011) Filters in topology optimization based on Helmholtz-type differential equations. *Int J Numer Methods Eng* 86(6):765-781. <https://doi.org/10.1002/nme.3072>
- Liu, JK, Chen, Q, Liang, X, To, AC (2019) Manufacturing cost constrained topology optimization for additive manufacturing. *Front Mech Eng* 14(2):213-221. <https://doi.org/10.1007/s11465-019-0536-z>
- Mass, Y, Amir, O (2017) Topology optimization for additive manufacturing: Accounting for overhang limitations using a virtual skeleton. *Addit Manuf* 18:58-73. <https://doi.org/10.1016/j.addma.2017.08.001>
- Mertens, R, Clijsters, S, Kempen, K, Kruth, J-P (2014) Optimization of Scan Strategies in Selective Laser Melting of Aluminum Parts With Downfacing Areas. 136(6):1-7. <https://doi.org/10.1115/1.4028620>
- Mezzadri, F, Qian, X (2020) A second-order measure of boundary oscillations for overhang control in topology optimization. 410:1-32. <https://doi.org/10.1016/j.jcp.2020.109365>
- Mhapsekar, K, McConaha, M, Anand, S (2018) Additive Manufacturing Constraints in Topology Optimization for Improved Manufacturability. *J Manuf Sci E-T Asme* 140(5):1-16. <https://doi.org/10.1115/1.4039198>
- Mirzendehdel, AM, Suresh, K (2016) Support structure constrained topology optimization for additive manufacturing. *Comput Aided Des* 81:1-13. <https://doi.org/10.1016/j.cad.2016.08.006>
- Olsen, J, Kim, IY (2020) Design for additive manufacturing: 3D simultaneous topology and build orientation optimization. *Struct Multidiscip Optim* 62(4):1989-2009. <https://doi.org/10.1007/s00158-020-02590-8>
- Panesar, A, Abdi, M, Hickman, D, Ashcroft, I (2018) Strategies for functionally graded lattice structures derived using topology optimisation for Additive Manufacturing. 19:81-94. <https://doi.org/https://doi.org/10.1016/j.addma.2017.11.008>
- Qian, XP (2017) Undercut and overhang angle control in topology optimization: A density gradient based integral approach. *Int J Numer Methods Eng* 111(3):247-272. <https://doi.org/10.1002/nme.5461>
- Ranjan, R, Samant, R, Anand, S (2017) Integration of Design for Manufacturing Methods With Topology Optimization in Additive Manufacturing. *J Manuf Sci Eng* 139(6):1-14. <https://doi.org/10.1115/1.4035216>
- Ryan, L, Kim, IY (2019) A multiobjective topology optimization approach for cost and time minimization in additive manufacturing. *Int J Numer Methods Eng* 118(7):371-394. <https://doi.org/10.1002/nme.6017>
- Sabiston, G, Kim, IY (2019) 3D topology optimization for cost and time minimization in additive manufacturing. *Struct Multidiscip Optim* 61(2):731-748. <https://doi.org/10.1007/s00158-019-02392-7>
- Sabiston, G, Kim, IY (2020) Void region restriction for additive manufacturing via a diffusion physics approach. *Int. J. Numer. Methods Eng.* 121(19):4347-4373. <https://doi.org/10.1002/nme.6434>
- Schmitt, M, Mehta, RM, Kim, IY (2020) Additive manufacturing infill optimization for automotive 3D-printed ABS components. *Rapid Prototyping J.* 26(1):89-99. <https://doi.org/10.1108/rpj-01-2019-0007>
- Sigmund, O (2007) Morphology-based black and white filters for topology optimization. *Struct Multidiscip Optim* 33:401-424. <https://doi.org/10.1007/s00158-006-0087-x>
- Sigmund, O (2022) On benchmarking and good scientific practise in topology optimization. *Struct Multidiscip Optim* 65(11):1-10. <https://doi.org/10.1007/s00158-022-03427-2>
- Svanberg, K (1987) The Method of Moving Asymptotes - a New Method for Structural Optimization. *Int J Numer Methods Eng* 24(2):359-373. <https://doi.org/10.1002/nme.1620240207>
- Thore, CJ, Grundstrom, HA, Torstenfelt, B, Klarbring, A (2019) Penalty regulation of overhang in topology optimization for additive manufacturing. *Struct Multidiscip Optim* 60(1):59-67. <https://doi.org/10.1007/s00158-019-02194-x>
- Verhoef, LA, Budde, BW, Chockalingam, C, García Nodar, B, van Wijk, AJM (2018) The effect of additive manufacturing on global energy demand: An assessment using a bottom-up approach. 112:349-360. <https://doi.org/10.1016/j.enpol.2017.10.034>

- Wang, C (2022) Simultaneous optimization of build orientation and topology for self-supported enclosed voids in additive manufacturing. *Comput Methods Appl Mech Eng* 388:1-20. <https://doi.org/10.1016/j.cma.2021.114227>
- Wang, C, Qian, X (2022) Simultaneous optimization of part and support for heat dissipation in additive manufacturing. 66(1):3. <https://doi.org/10.1007/s00158-022-03466-9>
- Wang, C, Wang, C, Yu, W, Lei, L, Yan, C, You, Y (2024) Achieving self-supported enclosed voids and machinable support structures in topology optimization for additive manufacturing. 67(8):142. <https://doi.org/10.1007/s00158-024-03858-z>
- Wang, C, Zhu, J, Zhang, W (2022) Simultaneous optimization of structural topology and build direction using B-spline parameterized density method. *Struct Multidiscip Optim* 65(11):1-20. <https://doi.org/10.1007/s00158-022-03422-7>
- Wang, CF, Qian, XP (2020) Simultaneous optimization of build orientation and topology for additive manufacturing. *Addit Manuf* 34:1-19. <https://doi.org/10.1016/j.addma.2020.101246>
- Wang, D, Yang, Y, Yi, Z, Su, X (2013) Research on the fabricating quality optimization of the overhanging surface in SLM process. 65(9):1471-1484. <https://doi.org/10.1007/s00170-012-4271-4>
- Wang, FW, Lazarov, BS, Sigmund, O (2011) On projection methods, convergence and robust formulations in topology optimization. *Struct. Multidiscip. Optim.* 43(6):767-784. <https://doi.org/10.1007/s00158-010-0602-y>
- Xu, B, Han, YS, Zhao, L, Xie, YM (2020) Topological optimization of continuum structures for additive manufacturing considering thin feature and support structure constraints. 53(12). <https://doi.org/10.1080/0305215x.2020.1849170>
- Zhu, J, Zhou, H, Wang, C, Zhou, L, Yuan, S, Zhang, W (2021) A review of topology optimization for additive manufacturing: Status and challenges. 34(1):91-110. <https://doi.org/10.1016/j.cja.2020.09.020>